
UNSUPERVISED DISCOVERY OF INTERMEDIATE PHASE ORDER IN THE FRUSTRATED J_1 - J_2 HEISENBERG MODEL VIA PROMETHEUS FRAMEWORK

PREPRINT

Brandon Yee,¹ Wilson Collins,¹ Maximilian Rutkowski,¹¹Physics Lab, Yee Collins Research Group

{b.yee, w.collins, r.rutkowski}@ycrg-labs.org

ABSTRACT

The spin-1/2 J_1 - J_2 Heisenberg model on the square lattice exhibits a debated intermediate phase between Néel antiferromagnetic and stripe ordered regimes, with competing theories proposing plaquette valence bond, nematic, and quantum spin liquid ground states. We apply the Prometheus variational autoencoder framework—previously validated on classical (2D, 3D Ising) and quantum (disordered transverse field Ising) phase transitions—to systematically explore the J_1 - J_2 phase diagram using a multi-scale approach. For $L = 4$, we employ exact diagonalization with full wavefunction analysis via quantum-aware VAE. For larger systems ($L = 6, 8$), we introduce a reduced density matrix (RDM) based methodology using DMRG ground states, enabling scaling beyond the exponential barrier of full Hilbert space representation. Through dense parameter scans of $J_2/J_1 \in [0, 1]$ and comprehensive latent space analysis, we identify the structure factor $S(\pi, \pi)$ and $S(\pi, 0)$ as the dominant order parameters discovered by the VAE, with correlations exceeding $|r| > 0.97$. The RDM-VAE approach successfully captures the Néel-to-stripe crossover near $J_2/J_1 \approx 0.5$ – 0.6 , demonstrating that local quantum correlations encoded in reduced density matrices contain sufficient information for unsupervised phase discovery. This work establishes a scalable pathway for applying machine learning to frustrated quantum systems where full wavefunction access is computationally prohibitive.

Keywords Quantum phase transitions · Frustrated magnetism · J1-J2 Heisenberg model · Variational autoencoders · Unsupervised learning · Reduced density matrices · DMRG

1 Introduction**1.1 The J_1 - J_2 Heisenberg Problem**

The spin-1/2 J_1 - J_2 Heisenberg model on the square lattice stands as one of the paradigmatic models in frustrated quantum magnetism, exhibiting rich physics arising from the competition between nearest-neighbor (J_1) and next-nearest-neighbor (J_2) antiferromagnetic interactions. The Hamiltonian is defined as

$$H = J_1 \sum_{\langle i,j \rangle} \vec{S}_i \cdot \vec{S}_j + J_2 \sum_{\langle\langle i,k \rangle\rangle} \vec{S}_i \cdot \vec{S}_k, \quad (1)$$

where \vec{S}_i are spin-1/2 operators, $J_1, J_2 > 0$ are antiferromagnetic coupling constants, and the sums run over nearest-neighbor and next-nearest-neighbor pairs respectively.

For small frustration ratio $J_2/J_1 \ll 1$, the ground state exhibits Néel antiferromagnetic order with staggered magnetization $\vec{m}_s = N^{-1} \sum_i (-1)^{i_x+i_y} \langle \vec{S}_i \rangle$ [1, 2]. For large frustration $J_2/J_1 \gg 1$, the system develops stripe (columnar) order where spins align ferromagnetically along one lattice direction and antiferromagnetically along the other [3]. The exact Majumdar-Ghosh point at $J_2/J_1 = 0.5$ in the one-dimensional variant admits an exact dimer ground state [1], but no such exact solution exists for the two-dimensional square lattice.

The intermediate regime $J_2/J_1 \sim 0.4\text{--}0.6$ has been the subject of intense theoretical and numerical investigation for over three decades, with no definitive consensus on the nature of the ground state. Competing proposals include:

- **Plaquette valence bond solid (VBS):** A state breaking lattice rotation symmetry with enhanced four-spin plaquette correlations [4].
- **Nematic order:** A state preserving spin-rotation symmetry but breaking lattice symmetries, characterized by directional spin correlations without magnetic order [3].
- **Quantum spin liquid:** An exotic state with no symmetry breaking and fractionalized excitations [5, 6, 7, 8].
- **Direct transition:** A scenario where no intermediate phase exists, with a continuous or weakly first-order transition directly from Néel to stripe order [9].

The resolution of this question carries significance beyond the specific J_1 - J_2 model. This system serves as the simplest frustrated quantum magnet on a bipartite lattice and provides insights into:

1. The role of quantum fluctuations in destroying classical magnetic order.
2. Mechanisms for emergent symmetries and exotic ground states in frustrated systems.
3. Connections to high-temperature superconductivity, where similar frustration patterns appear in the parent antiferromagnetic compounds [2].
4. Experimental realizations in organic salts [10], layered cuprates, and cold atom quantum simulators [11].

1.2 Computational Challenges and the Scaling Problem

The determination of the intermediate phase structure faces several computational obstacles that have prevented definitive resolution despite decades of study.

Finite system sizes and exponential scaling. Exact diagonalization (ED) provides numerically exact ground states but is limited by the exponential scaling of the Hilbert space dimension (2^N for N spins). State-of-the-art ED calculations on the square lattice are restricted to $N \lesssim 40$ spins ($\sim 6 \times 6$ lattice) [12], where finite-size effects can be substantial, particularly in frustrated systems with competing orders. For a 4×4 lattice, the $S_{\text{tot}}^z = 0$ sector has dimension $\binom{16}{8} = 12,870$, which is tractable. However, for $L = 6$ ($N = 36$ spins), this grows to $\binom{36}{18} \approx 9.1 \times 10^9$, and for $L = 8$ ($N = 64$ spins), to $\binom{64}{32} \approx 1.8 \times 10^{18}$ —far beyond any direct diagonalization capability.

Sign problem in quantum Monte Carlo. While quantum Monte Carlo (QMC) can access larger system sizes, frustrated Heisenberg models typically suffer from the fermion sign problem after Jordan-Wigner transformation, leading to exponentially poor signal-to-noise ratio that limits accessible temperatures and system sizes [12].

DMRG convergence issues. Density matrix renormalization group (DMRG) methods can handle larger 2D systems through cylindrical geometries [13, 14], but convergence in frustrated systems is sensitive to initial conditions, bond dimension truncation, and boundary effects. Different initialization schemes can converge to different local minima in the energy landscape [7]. Crucially, while DMRG provides expectation values and reduced density matrices, the full wavefunction in the computational basis remains inaccessible—DMRG does not provide the exponentially large coefficient vector $|\psi\rangle = \sum_{\sigma} c_{\sigma} |\sigma\rangle$.

Unknown order parameters. Traditional analysis relies on computing correlators for hypothesized order parameters. When the nature of the phase is genuinely unknown—as in the J_1 - J_2 intermediate regime—one may not know which observables to measure. Systematically exploring all possible order parameters is computationally prohibitive and may miss exotic order types with no simple local characterization.

The machine learning bottleneck. Previous applications of variational autoencoders to quantum phase transitions, including our own Prometheus framework [15, 16], have relied on full wavefunction access. The Q-VAE architecture takes the wavefunction coefficients $\{c_{\sigma}\}$ as input and learns compressed latent representations. This approach is fundamentally limited to system sizes where the full wavefunction can be stored and manipulated—typically $N \lesssim 20\text{--}24$ spins.

This creates a critical gap: the most interesting physics in frustrated systems often emerges only at larger system sizes where finite-size effects are reduced, but the machine learning tools developed for phase discovery cannot access these scales.

These challenges motivate the development of alternative approaches that can identify phase boundaries and characterize phases without prior knowledge of the order parameter structure, while also scaling beyond the exponential barrier of full wavefunction methods.

1.3 The RDM-VAE Solution

In this work, we bridge this gap by introducing a reduced density matrix (RDM) based approach to variational autoencoder analysis. The key insight is that local quantum correlations—which determine phase structure and order parameters—are encoded in the reduced density matrices of small subsystems, not in the global phase relationships of the full wavefunction.

For a subsystem A of n_A sites, the reduced density matrix is

$$\rho_A = \text{Tr}_B |\psi\rangle\langle\psi|, \quad (2)$$

where B is the complement of A . The dimension of ρ_A scales as $2^{n_A} \times 2^{n_A}$, which for small subsystems ($n_A \lesssim 4-6$) remains tractable regardless of total system size. Crucially, DMRG can efficiently compute these reduced density matrices even for systems with $N = 64$ or more spins.

Our RDM-VAE approach proceeds in four stages: first, we extract reduced density matrices from DMRG ground states for representative subsystems including single sites, nearest-neighbor pairs, next-nearest-neighbor pairs, and 2×2 plaquettes; second, we flatten and concatenate these RDM elements into a feature vector; third, we train a standard VAE on these RDM features; and finally, we analyze the latent space for phase structure and order parameter discovery.

This methodology enables scaling to $L = 6$ and $L = 8$ lattices while preserving the unsupervised learning paradigm that makes Prometheus effective for phase discovery.

1.4 Machine Learning for Phase Discovery

Machine learning has emerged as a powerful tool for studying phase transitions in condensed matter systems, with approaches broadly classified into supervised and unsupervised methods.

Supervised approaches train neural networks on labeled configurations (assigned to known phases) and achieve remarkable classification accuracy. Carrasquilla and Melko [17] demonstrated that convolutional neural networks trained on Monte Carlo configurations of the 2D Ising model can classify phases and locate the critical temperature. Van Nieuwenburg et al. [18] introduced a semi-supervised “learning by confusion” approach that identifies phase boundaries by training classifiers on different parameter regimes and finding regions where they disagree. These methods have been successfully applied to quantum systems [19], topological phases [20], and many-body localization [21].

However, supervised methods face a fundamental limitation: they require labeled training data, which presupposes knowledge of the phase structure—precisely the information one seeks to discover in novel systems. For the J_1 - J_2 intermediate regime, we do not know the correct phase labels, making supervised classification circular.

Unsupervised methods attempt to discover phase structure from unlabeled data. Wang [22] showed that principal component analysis (PCA) applied to classical Ising configurations yields leading components that correlate with the magnetization order parameter. Wetzel [23] extended this approach using variational autoencoders (VAEs), demonstrating that learned latent representations naturally organize according to phase structure. Rodriguez-Nieva and Scheurer [24] developed interpretable unsupervised learning methods for topological phases, showing that neural networks can discover topological invariants without supervision.

Despite these successes, most unsupervised studies have focused on *validating* the method on systems with known phase diagrams rather than *discovering* genuinely unknown physics. The critical question remains: *Can unsupervised machine learning discover novel quantum phases when applied to open problems where the phase structure is uncertain?*

1.5 The Prometheus Framework

To address this question, we have developed Prometheus, a systematic framework for unsupervised discovery of phase transitions using variational autoencoders, and validated it through a progression of increasingly complex systems.

2D Ising model validation (Yee et al., 2026a). We first established the Prometheus methodology on the exactly solvable 2D Ising model [15], where the exact solution provides unambiguous ground truth. Using physics-informed training procedures including symmetry-preserving augmentation and progressive training schedules, we demonstrated automated order parameter discovery correlating with theoretical magnetization, critical temperature detection near the exact Onsager value, and improvement over principal component analysis. This validation on an exactly solvable system established that the VAE latent space naturally captures order parameter physics when trained with appropriate inductive biases, without requiring any labeled phase information or prior knowledge of the magnetization as the relevant degree of freedom.

Extension to 3D and quantum systems (Yee et al., 2026b). Having established baseline performance on a solvable system, we extended Prometheus to cases without exact solutions [16], addressing two critical questions: (1) Does the method work when there is no analytical solution to validate against? (2) Can it detect qualitatively different types of critical behavior?

For the 3D classical Ising model, which has no known exact solution, we demonstrated critical temperature detection in agreement with high-precision Monte Carlo benchmarks and critical exponent extraction consistent with the 3D Ising universality class.

For the one-dimensional disordered transverse field Ising model (DTFIM), we demonstrated detection of exotic quantum critical behavior fundamentally different from classical phase transitions, including quantum critical point detection at zero disorder and the first unsupervised detection of activated scaling, successfully distinguishing between conventional power-law scaling (clean system) and activated scaling (disordered system).

The quantum extension introduced several key methodological advances:

1. **Quantum-aware VAE (Q-VAE) architecture:** Modified encoder-decoder to handle complex-valued wavefunctions $|\psi\rangle = \sum_{\sigma} c_{\sigma} |\sigma\rangle$ with proper normalization $\langle\psi|\psi\rangle = 1$.
2. **Fidelity-based loss function:** Replacement of mean squared error with quantum fidelity $F = |\langle\psi_{\text{in}}|\psi_{\text{recon}}\rangle|^2$ to respect quantum mechanical structure.
3. **Disorder averaging protocols:** Systematic averaging over disorder realizations with bootstrap uncertainty quantification.
4. **Activated scaling detection:** Framework for distinguishing power-law vs. activated critical behavior through latent correlation length analysis.

This systematic progression—exact solution \rightarrow numerical-only solution \rightarrow exotic quantum criticality—established Prometheus as a validated tool with demonstrated capability to:

- Discover order parameters without supervision
- Work in the absence of exact analytical solutions
- Detect qualitatively different types of critical phenomena
- Extract quantitative critical properties with controlled uncertainties

Having built confidence through validation on known systems, we are now positioned to apply Prometheus to an open question: *What is the nature of the intermediate phase in the J_1 - J_2 Heisenberg model?*

1.6 This Work: Multi-Scale Discovery

In this work, we deploy a multi-scale approach to the J_1 - J_2 Heisenberg model combining two complementary methodologies:

1. **Comprehensive exact diagonalization ($L = 4$):** Ground state calculations for a 4×4 lattice across a dense scan of frustration ratios $J_2/J_1 \in [0.3, 0.7]$ with step size $\Delta(J_2/J_1) = 0.01$, yielding 41 ground states.
2. **DMRG with RDM-VAE ($L = 6, 8$):** Ground state calculations using density matrix renormalization group for 6×6 and 8×8 lattices across $J_2/J_1 \in [0, 1]$ with step size 0.025, yielding 41 ground states per system size.
3. **Quantum-aware variational autoencoder analysis:** Application of the Q-VAE architecture with fidelity-based loss function to learn compressed latent representations of the full ground state wavefunctions $|\psi(J_2/J_1)\rangle$ for $L = 4$.
4. **RDM-VAE analysis:** Application of the new RDM-VAE architecture to learn compressed latent representations of reduced density matrix features for $L = 6, 8$.
5. **Unsupervised order parameter discovery:** Systematic Pearson correlation analysis between latent dimensions and 11 physical observables (staggered magnetization, stripe order, plaquette order, nematic order, dimer order, structure factors at key wavevectors, energy density, and entanglement entropy) with bootstrap confidence intervals and permutation tests for statistical significance.
6. **Phase boundary detection:** Three independent methods—latent variance peaks, reconstruction error maxima, and fidelity susceptibility—combined via inverse-variance weighted ensemble estimation.

7. **Validation framework:** Automated validation in known Néel and stripe phases, requiring correlation $|r| \geq 0.7$ with expected order parameters, plus comparison with literature critical point bounds.

This progression allows us to: (1) validate that RDM features capture the same physics as full wavefunctions by comparing $L = 4$ results; (2) access larger system sizes where the intermediate phase structure may be more clearly resolved; and (3) establish a scalable methodology for future applications to even larger systems.

Our approach represents a fundamentally different paradigm from previous applications of machine learning to physics: rather than using ML to validate known physics or using physics to validate ML methods, we apply a *rigorously validated ML tool to solve an open physics problem*. The three-paper validation sequence establishes credibility that allows discovery claims to be taken seriously.

1.7 Organization

The remainder of this paper is organized as follows. Section 2 reviews related work on machine learning for phase transitions and the J_1 - J_2 model. Section 3 describes our computational methodology, including exact diagonalization procedures (Sec. 3.2), DMRG ground state generation (Sec. 3.3), the quantum-aware VAE architecture (Sec. 3.4), the RDM-VAE architecture (Sec. 3.5), order parameter discovery protocols (Sec. 3.6), and critical point detection methods (Sec. 3.7). Section 4 presents our results for all system sizes. Section 5 discusses their implications in the context of the J_1 - J_2 debate. Section 6 concludes. Detailed technical specifications are provided in the Appendices. All code and data will be made publicly available to enable community validation and extension of this work.

2 Related Work

2.1 Machine Learning for Phase Transitions

The application of machine learning to phase transitions has grown rapidly over the past decade, with approaches spanning supervised classification, unsupervised discovery, and generative modeling.

Supervised methods have demonstrated remarkable success in phase classification. Carrasquilla and Melko [17] showed that convolutional neural networks trained on Monte Carlo configurations of the 2D Ising model can classify phases and locate the critical temperature with high accuracy. This work sparked widespread interest in neural network approaches to condensed matter physics. Van Nieuwenburg et al. [18] introduced a semi-supervised “learning by confusion” approach that identifies phase boundaries by training classifiers on different parameter regimes and finding regions of maximum confusion. Subsequent work extended these methods to quantum systems [19], topological phases [20], and many-body localization [21].

Unsupervised methods offer the advantage of not requiring labeled training data. Wang [22] demonstrated that principal component analysis (PCA) applied to classical Ising configurations yields leading components that correlate with the magnetization order parameter. Wetzel [23] extended this approach using variational autoencoders (VAEs), showing that learned latent representations naturally organize according to phase structure. Hu et al. [25] applied restricted Boltzmann machines to discover phase transitions without supervision. Rodriguez-Nieva and Scheurer [24] developed interpretable unsupervised learning methods for topological phases, demonstrating that neural networks can discover topological invariants.

More recent work has explored the theoretical foundations of why machine learning succeeds at phase detection. Mehta and Schwab [26] established connections between restricted Boltzmann machines and renormalization group transformations. Koch-Janusz and Ringel [27] showed that neural networks can learn relevant degrees of freedom in a manner analogous to real-space renormalization. These theoretical insights provide a foundation for understanding the success of data-driven approaches to phase discovery.

2.2 Numerical Studies of the J_1 - J_2 Model

The J_1 - J_2 Heisenberg model has been studied extensively using a variety of numerical methods, each with distinct strengths and limitations.

Exact diagonalization studies [28, 29] provided early evidence for an intermediate phase but were limited to small system sizes ($N \lesssim 36$). These studies established the basic phase diagram with Néel order at small J_2/J_1 and stripe order at large J_2/J_1 , but could not definitively characterize the intermediate regime.

Quantum Monte Carlo methods face the sign problem for frustrated systems, limiting their applicability. However, specialized techniques such as the stochastic series expansion with directed loop updates [12] have been applied to related unfrustrated models, providing benchmarks for other methods.

Density matrix renormalization group (DMRG) studies [13, 14] have accessed larger system sizes through cylindrical geometries. Jiang et al. [6] reported DMRG evidence for a spin liquid phase in the intermediate regime, while Gong et al. [7] found results consistent with either a narrow spin liquid or a direct first-order transition. Mambrini et al. [30] provided exact diagonalization evidence for plaquette valence bond solid order, and Wang et al. [31] used PEPS variational states to argue for a gapless spin liquid ground state. The sensitivity of results to boundary conditions, bond dimension, and method has contributed to the ongoing debate.

Variational Monte Carlo with tensor network states [8, 9] has provided additional perspectives, with Ferrari and Becca [9] finding spectral signatures consistent with a direct or weakly first-order transition, while Hu et al. [8] argued for a gapless spin liquid ground state. The lack of consensus across methods reflects the genuine difficulty of the problem.

2.3 The Prometheus Framework

Our Prometheus framework represents a systematic approach to unsupervised phase discovery, validated through a progression of increasingly complex systems.

In our first study [15], we established the methodology on the exactly solvable 2D Ising model, demonstrating automated order parameter discovery, critical temperature detection near the exact Onsager value, and improvement over PCA baselines. This validation on an exactly solvable system established that VAE latent spaces naturally capture order parameter physics when trained with appropriate inductive biases.

Our second study [16] extended Prometheus to systems without exact solutions: the 3D classical Ising model and the one-dimensional disordered transverse field Ising model (DTFIM). For the 3D Ising model, we demonstrated critical temperature detection in agreement with Monte Carlo benchmarks. For the DTFIM, we achieved the first unsupervised detection of activated scaling, successfully distinguishing between conventional power-law scaling and the exotic activated scaling characteristic of infinite-randomness fixed points.

The quantum extension introduced the quantum-aware VAE (Q-VAE) architecture with fidelity-based loss functions, enabling application to quantum ground state wavefunctions. This systematic validation sequence—exact solution, numerical-only solution, exotic quantum criticality—establishes the credibility necessary for applying Prometheus to open problems.

2.4 Reduced Density Matrix Approaches

The use of reduced density matrices (RDMs) for characterizing quantum phases has a long history in quantum chemistry and condensed matter physics. The n -representability problem [32] established fundamental constraints on physically realizable RDMs. More recently, RDMs have been used as inputs for machine learning models in quantum chemistry [33] and materials science.

In the context of phase transitions, entanglement entropy—computed from the spectrum of reduced density matrices—has emerged as a powerful diagnostic [34, 35]. Area law scaling of entanglement entropy characterizes gapped phases, while logarithmic corrections indicate critical points or topological order.

Our RDM-VAE approach builds on these foundations by using the full RDM elements (not just the entanglement spectrum) as input features for unsupervised learning. This preserves information about local correlations while enabling scaling beyond the exponential barrier of full wavefunction methods.

3 Methods

3.1 The J_1 - J_2 Heisenberg Model

We study the spin-1/2 J_1 - J_2 Heisenberg antiferromagnet on square lattices of linear sizes $L = 4, 6, 8$ with periodic boundary conditions, defined by the Hamiltonian of Eq. (1). Throughout this work, we set $J_1 = 1$ as the energy scale and vary the frustration ratio J_2/J_1 .

The Hilbert space dimension for a system of $N = L \times L$ spins is $\dim(\mathcal{H}) = 2^N$. To make the problem tractable, we exploit conservation of total S^z (the z -component of total spin). The $S_{\text{tot}}^z = 0$ sector, which contains the ground state

for antiferromagnetic systems, has dimension

$$\dim(\mathcal{H}_{S^z=0}) = \binom{N}{N/2}, \quad (3)$$

providing a significant reduction from the full Hilbert space. For $L = 4$, this gives 12,870 states; for $L = 6$, approximately 9.1×10^9 states; for $L = 8$, approximately 1.8×10^{18} states.

3.2 Exact Diagonalization for $L = 4$

3.2.1 Ground State Computation

We compute ground states $|\psi_0(J_2/J_1, L)\rangle$ using the Lanczos iterative diagonalization algorithm, implemented via the QuSpin Python package [36, 37] combined with SciPy’s ARPACK-based eigsh solver. The Lanczos method constructs a Krylov subspace through repeated application of the Hamiltonian matrix to an initial random state:

$$\mathcal{K}_n = \text{span}\{|v_0\rangle, H|v_0\rangle, H^2|v_0\rangle, \dots, H^{n-1}|v_0\rangle\}, \quad (4)$$

and diagonalizes the Hamiltonian within this subspace, yielding approximate eigenvalues and eigenvectors.

For the frustrated Heisenberg model, we construct the Hamiltonian in the $S_{\text{tot}}^z = 0$ sector using QuSpin’s `spin_basis_general` with $N_{\text{up}} = N/2$. The nearest-neighbor and next-nearest-neighbor interaction terms $\vec{S}_i \cdot \vec{S}_j$ are decomposed as:

$$\vec{S}_i \cdot \vec{S}_j = S_i^z S_j^z + \frac{1}{2}(S_i^+ S_j^- + S_i^- S_j^+), \quad (5)$$

where $S^\pm = S^x \pm iS^y$ are spin raising and lowering operators. The $S_i^z S_j^z$ terms contribute to the diagonal, while the $S^+ S^-$ terms produce off-diagonal matrix elements connecting basis states that differ by a single spin flip.

The Hamiltonian is stored in Compressed Sparse Row (CSR) format. Nearest-neighbor bonds connect sites (i_x, i_y) to $(i_x + 1, i_y)$ and $(i_x, i_y + 1)$ with periodic boundary conditions. Next-nearest-neighbor bonds connect to diagonal neighbors $(i_x \pm 1, i_y + 1)$. The Lanczos iteration proceeds until the ground state energy converges, defined by the criterion:

$$|E_n - E_{n-1}| < \epsilon_{\text{tol}} = 10^{-10}, \quad (6)$$

with a maximum of 1000 iterations. The final ground state wavefunction $|\psi_0\rangle$ is explicitly normalized to $\langle\psi_0|\psi_0\rangle = 1$, with validation that $|\langle\psi_0|\psi_0\rangle - 1| < 10^{-8}$.

3.2.2 Parameter Sweep Protocol

For the $L = 4$ lattice, we perform a systematic sweep over frustration ratios:

$$J_2/J_1 \in [0.3, 0.7], \quad (7)$$

$$\Delta(J_2/J_1) = 0.01. \quad (8)$$

This yields 41 parameter points. The parameter range focuses computational resources on the debated intermediate regime while including sufficient margin into the Néel ($J_2/J_1 < 0.4$) and stripe ($J_2/J_1 > 0.6$) regimes for validation.

At each parameter point J_2/J_1 , we perform an independent ground state calculation. The pipeline supports parallel execution across parameter points using Python’s `multiprocessing.Pool` with 6 processes, with checkpointing to enable resumption. Memory monitoring and garbage collection are performed between computations.

3.2.3 Observable Computation

For each ground state $|\psi_0\rangle$, we compute a comprehensive set of physical observables exactly from wavefunction coefficients using QuSpin operators, without Monte Carlo sampling. Key quantities include:

Energy and energy density:

$$E = \langle\psi_0|H|\psi_0\rangle, \quad e = E/N. \quad (9)$$

Staggered magnetization (Néel order parameter): In the $S^z = 0$ sector, $\langle S_i^z \rangle = 0$ everywhere, so we compute via spin-spin correlations:

$$m_s^2 = \frac{1}{N^2} \sum_{i,j} (-1)^{i_x+i_y+j_x+j_y} \langle \vec{S}_i \cdot \vec{S}_j \rangle, \quad m_s = \sqrt{|m_s^2|}. \quad (10)$$

Stripe order parameter: The maximum of x -direction and y -direction columnar magnetization:

$$m_{\text{stripe}} = \max \left\{ \sqrt{|\langle M_x \rangle|^2}, \sqrt{|\langle M_y \rangle|^2} \right\}, \quad (11)$$

where $M_x = N^{-1} \sum_i (-1)^{i_x} \vec{S}_i$ and $M_y = N^{-1} \sum_i (-1)^{i_y} \vec{S}_i$.

Plaquette order parameter: Four-spin correlations on elementary plaquettes:

$$P = \frac{1}{N_p} \sum_p \langle \vec{S}_1 \cdot \vec{S}_2 \rangle_p \langle \vec{S}_3 \cdot \vec{S}_4 \rangle_p, \quad (12)$$

where the sum runs over all $N_p = L^2$ plaquettes with periodic boundary conditions.

Nematic order: Anisotropy between x and y bond correlations:

$$Q = \left| \frac{1}{N} \sum_i \langle \vec{S}_i \cdot \vec{S}_{i+\hat{x}} \rangle - \frac{1}{N} \sum_i \langle \vec{S}_i \cdot \vec{S}_{i+\hat{y}} \rangle \right|. \quad (13)$$

Dimer order: Alternating bond strength pattern:

$$D = \frac{1}{2N} \left| \sum_i (-1)^{i_x+i_y} \left(\langle \vec{S}_i \cdot \vec{S}_{i+\hat{x}} \rangle + \langle \vec{S}_i \cdot \vec{S}_{i+\hat{y}} \rangle \right) \right|. \quad (14)$$

Structure factor at ordering wavevectors $\vec{q} \in \{(\pi, \pi), (\pi, 0), (0, \pi)\}$:

$$S(\vec{q}) = \frac{1}{N} \sum_{i,j} e^{i\vec{q} \cdot (\vec{r}_i - \vec{r}_j)} \langle \vec{S}_i \cdot \vec{S}_j \rangle. \quad (15)$$

Entanglement entropy: Computed via singular value decomposition of the wavefunction reshaped as a bipartite matrix:

$$S_A = - \sum_k \lambda_k^2 \log \lambda_k^2, \quad (16)$$

where λ_k are the singular values.

3.3 DMRG Ground States for $L = 6, 8$

For larger lattices where exact diagonalization is infeasible, we employ the density matrix renormalization group (DMRG) method to compute ground states.

3.3.1 DMRG Implementation

Ground states are computed using matrix product state (MPS) representations with bond dimension $\chi = 200\text{--}400$, increased until energy convergence is achieved. The DMRG algorithm performs 10–20 sweeps with convergence criterion $\Delta E < 10^{-8}$ between successive sweeps. We use cylindrical boundary conditions with periodic boundaries along one direction to reduce finite-size effects while maintaining computational tractability.

3.3.2 Parameter Sweep Protocol

For $L = 6$ and $L = 8$ lattices, we perform systematic sweeps over the full frustration range:

$$J_2/J_1 \in [0, 1], \quad (17)$$

$$\Delta(J_2/J_1) = 0.025. \quad (18)$$

This yields 41 parameter points per system size, covering the complete phase diagram from pure Néel ($J_2/J_1 = 0$) through the intermediate regime to pure stripe ($J_2/J_1 = 1$).

3.3.3 RDM Extraction

From each DMRG ground state, we extract reduced density matrices for representative subsystems. Table 1 summarizes the RDM types included in the feature vector.

Table 1: Reduced density matrix types extracted from DMRG ground states. The total feature dimension d_{RDM} depends on lattice size due to the number of bonds and plaquettes.

RDM Type	Matrix Dimension	Count ($L = 6$)	Count ($L = 8$)
Single-site ρ_i	2×2	36	64
Nearest-neighbor ρ_{ij}	4×4	72	128
Next-nearest-neighbor ρ_{ik}	4×4	72	128
Plaquette ρ_{\square}	16×16	36	64
Total feature dimension	—	706	2148

The RDM feature vector is constructed by flattening and concatenating these matrices:

$$\vec{x}_{\text{RDM}} = [\text{vec}(\rho_1), \text{vec}(\rho_2), \dots, \text{vec}(\rho_{ij}), \text{vec}(\rho_{\square,1}), \dots] \in \mathbb{R}^{d_{\text{RDM}}}. \quad (19)$$

The key insight is that these RDM elements encode local quantum correlations—spin-spin correlations, entanglement structure, and local order—which are precisely the quantities that distinguish different quantum phases. By learning compressed representations of RDM features, the VAE discovers the relevant degrees of freedom for phase classification without requiring the full wavefunction.

3.4 Quantum-Aware Variational Autoencoder

The quantum-aware VAE (Q-VAE) architecture employed for $L = 4$ is adapted from our previous study of the disordered transverse field Ising model [16], with modifications to accommodate the different Hilbert space structure of the Heisenberg model.

3.4.1 Wavefunction Representation

A quantum ground state $|\psi_0\rangle$ is represented as a complex-valued vector in the computational (S^z) basis:

$$|\psi_0\rangle = \sum_{\sigma} c_{\sigma} |\sigma\rangle, \quad c_{\sigma} \in \mathbb{C}, \quad \langle \psi_0 | \psi_0 \rangle = 1, \quad (20)$$

where $|\sigma\rangle$ are basis states in the $S_{\text{tot}}^z = 0$ sector.

To interface with real-valued neural networks, we represent the wavefunction as a real vector by concatenating the real and imaginary parts:

$$\vec{x} = [\text{Re}(c_1), \dots, \text{Re}(c_D), \text{Im}(c_1), \dots, \text{Im}(c_D)] \in \mathbb{R}^{2D}, \quad (21)$$

where $D = \dim(\mathcal{H}_{S^z=0}) = 12,870$ for $L = 4$.

3.4.2 Encoder Architecture

The encoder network $q_{\phi}(\vec{z}|\vec{x})$ maps the high-dimensional wavefunction to a low-dimensional latent space via three fully-connected layers with layer normalization and ReLU activation:

$$\begin{aligned} \vec{h}_1 &= \text{ReLU}(\text{LayerNorm}(\mathbf{W}_1 \vec{x} + \vec{b}_1)), & \dim(\vec{h}_1) &= 512, \\ \vec{h}_2 &= \text{ReLU}(\text{LayerNorm}(\mathbf{W}_2 \vec{h}_1 + \vec{b}_2)), & \dim(\vec{h}_2) &= 256, \\ \vec{h}_3 &= \text{ReLU}(\text{LayerNorm}(\mathbf{W}_3 \vec{h}_2 + \vec{b}_3)), & \dim(\vec{h}_3) &= 128, \\ \vec{\mu} &= \mathbf{W}_{\mu} \vec{h}_3 + \vec{b}_{\mu}, & \dim(\vec{\mu}) &= d_z, \\ \log \vec{\sigma}^2 &= \mathbf{W}_{\sigma} \vec{h}_3 + \vec{b}_{\sigma}, & \dim(\log \vec{\sigma}^2) &= d_z, \end{aligned} \quad (22)$$

outputting parameters $(\vec{\mu}, \vec{\sigma}^2)$ of a diagonal Gaussian distribution:

$$q_{\phi}(\vec{z}|\vec{x}) = \mathcal{N}(\vec{z}; \vec{\mu}(\vec{x}), \text{diag}(\vec{\sigma}^2(\vec{x}))), \quad (23)$$

with latent dimension $d_z = 8$ by default.

3.4.3 Reparameterization and Decoder

Latent vectors are sampled using the reparameterization trick [38]:

$$\vec{z} = \vec{\mu} + \vec{\sigma} \odot \vec{\epsilon}, \quad \vec{\epsilon} \sim \mathcal{N}(\vec{0}, \mathbf{I}). \quad (24)$$

The decoder network $p_\theta(\vec{x}|\vec{z})$ reconstructs the wavefunction through a symmetric architecture with hidden layers [128, 256, 512], each with LayerNorm and ReLU. The final layer outputs dimension $2D$, followed by explicit wavefunction normalization:

$$\psi_{\text{norm}} = \frac{\psi_{\text{out}}}{\sqrt{\sum_i (|\text{Re}(\psi_i)|^2 + |\text{Im}(\psi_i)|^2) + \epsilon}}, \quad (25)$$

where $\epsilon = 10^{-10}$ ensures numerical stability, enforcing $\langle \psi_{\text{recon}} | \psi_{\text{recon}} \rangle = 1$.

3.4.4 Fidelity-Based Loss Function

The quantum fidelity between input and reconstructed states is computed as:

$$F(|\psi_{\text{in}}\rangle, |\psi_{\text{recon}}\rangle) = |\langle \psi_{\text{in}} | \psi_{\text{recon}} \rangle|^2. \quad (26)$$

For wavefunctions represented as $[\text{Re}(\psi), \text{Im}(\psi)]$, the complex inner product is:

$$\langle \psi_{\text{in}} | \psi_{\text{recon}} \rangle = \sum_i (\text{Re}(\psi_{\text{in}})_i \text{Re}(\psi_{\text{recon}})_i + \text{Im}(\psi_{\text{in}})_i \text{Im}(\psi_{\text{recon}})_i) + i \sum_i (\text{Re}(\psi_{\text{in}})_i \text{Im}(\psi_{\text{recon}})_i - \text{Im}(\psi_{\text{in}})_i \text{Re}(\psi_{\text{recon}})_i). \quad (27)$$

The fidelity loss is:

$$\mathcal{L}_{\text{fidelity}} = 1 - F(|\psi_{\text{in}}\rangle, |\psi_{\text{recon}}\rangle). \quad (28)$$

The complete training objective is the evidence lower bound:

$$\mathcal{L}_{\text{ELBO}} = \mathbb{E}_{q_\phi(\vec{z}|\vec{x})}[\mathcal{L}_{\text{fidelity}}] + \beta D_{\text{KL}}(q_\phi(\vec{z}|\vec{x}) \| p(\vec{z})), \quad (29)$$

where $p(\vec{z}) = \mathcal{N}(\vec{0}, \mathbf{I})$ is the standard normal prior, $\beta = 0.1$ is the KL weight, and the KL divergence has closed form:

$$D_{\text{KL}} = -\frac{1}{2} \sum_{k=1}^{d_z} (1 + \log \sigma_k^2 - \mu_k^2 - \sigma_k^2). \quad (30)$$

3.4.5 Training Procedure

The Q-VAE is trained using the Adam optimizer [39] with learning rate $\eta = 10^{-3}$ and cosine annealing schedule. Training hyperparameters include: batch size 32 (or smaller if dataset size requires), maximum epochs 1000, early stopping patience 50 epochs without validation improvement, gradient clipping with max norm 1.0, and train/validation split 80%/20%.

Data augmentation exploits the S^z symmetry of the Heisenberg Hamiltonian. For a wavefunction $[\text{Re}(\psi), \text{Im}(\psi)]$, the S^z flip corresponds to complex conjugation $\psi \rightarrow \psi^*$, mapping $[\text{Re}(\psi), \text{Im}(\psi)] \rightarrow [\text{Re}(\psi), -\text{Im}(\psi)]$. This augmentation is applied with 50% probability during training.

The best model state (lowest validation loss) is saved and restored after training completes. All tensor operations include explicit checks for NaN/Inf values to ensure numerical stability.

3.5 RDM-VAE Architecture

The RDM-VAE is a standard variational autoencoder adapted for RDM feature inputs, used for $L = 6$ and $L = 8$ where full wavefunction access is infeasible.

3.5.1 Encoder Architecture

The encoder network maps the RDM feature vector to a low-dimensional latent space:

$$\begin{aligned} \vec{h}_1 &= \text{ReLU}(\text{LayerNorm}(\mathbf{W}_1 \vec{x}_{\text{RDM}} + \vec{b}_1)), & \dim(\vec{h}_1) &= 256, \\ \vec{h}_2 &= \text{ReLU}(\text{LayerNorm}(\mathbf{W}_2 \vec{h}_1 + \vec{b}_2)), & \dim(\vec{h}_2) &= 128, \\ \vec{h}_3 &= \text{ReLU}(\text{LayerNorm}(\mathbf{W}_3 \vec{h}_2 + \vec{b}_3)), & \dim(\vec{h}_3) &= 64, \\ \vec{\mu}, \log \vec{\sigma}^2 &= \text{Linear}(\vec{h}_3), & \dim &= d_z = 8. \end{aligned} \quad (31)$$

3.5.2 Decoder Architecture

The decoder uses a symmetric architecture [64, 128, 256] reconstructing \vec{x}_{RDM} .

3.5.3 Loss Function

For RDM features, we use mean squared error reconstruction (not fidelity, since RDMs are real-valued density matrix elements):

$$\mathcal{L}_{\text{RDM}} = \|\vec{x}_{\text{RDM}} - \vec{x}_{\text{recon}}\|^2 + \beta D_{\text{KL}}(q_{\phi}(\vec{z}|\vec{x})\|p(\vec{z})), \quad (32)$$

with $\beta = 0.1$ and standard normal prior $p(\vec{z}) = \mathcal{N}(\vec{0}, \mathbf{I})$.

3.5.4 Training Procedure

The RDM-VAE is trained with the same hyperparameters as the Q-VAE: Adam optimizer with learning rate 10^{-3} , batch size 32, maximum 1000 epochs, early stopping patience 50 epochs, and 80%/20% train/validation split.

3.6 Order Parameter Discovery

3.6.1 Latent Space Encoding

After training, each ground state is encoded to its deterministic latent representation $\vec{z}(J_2/J_1, L) = \vec{\mu}(\vec{x})$ (the mean of the latent distribution, without sampling). This provides a compressed representation of the quantum state suitable for analysis.

3.6.2 Latent Space Structure Analysis

We characterize the latent space structure through several metrics:

Latent variance: For each J_2/J_1 value, we compute the variance of latent representations:

$$\chi_z(J_2/J_1) = \sum_{k=1}^{d_z} \text{Var}[z_k(J_2/J_1)], \quad (33)$$

where the sum is over latent dimensions. Peaks in χ_z indicate critical regions where the latent representation changes most rapidly.

Trajectory arc length: The total arc length of the latent trajectory measures smoothness of evolution:

$$\ell = \sum_i \|\vec{z}(J_2/J_1^{(i+1)}) - \vec{z}(J_2/J_1^{(i)})\|_2. \quad (34)$$

Discontinuities (jumps exceeding $2 \times$ median step size) may indicate phase transitions.

Dimensionality reduction: t-SNE and UMAP projections visualize latent structure in 2D.

3.6.3 Correlation with Physical Observables

We compute Pearson correlations between each latent dimension z_k and physical observables \mathcal{O} :

$$r(z_k, \mathcal{O}) = \frac{\text{Cov}(z_k, \mathcal{O})}{\sigma_{z_k} \sigma_{\mathcal{O}}}. \quad (35)$$

Statistical significance is assessed via: hypothesis testing with significance level $\alpha = 0.01$, bootstrap confidence intervals (1000 resamples, 95% CI), and permutation tests (10000 permutations) for robust p -values.

Correlations with $|r| \geq 0.8$ and $p < 0.01$ are considered significant. We test correlations with all computed observables: staggered magnetization, stripe order, plaquette order, dimer order, nematic order, structure factors, energy density, and entanglement entropy.

3.6.4 Order Parameter Mapping

For each latent dimension showing significant correlations, we identify the most strongly correlated observable as the ‘‘discovered’’ order parameter. This mapping is validated by checking that:

1. In the Néel regime ($J_2/J_1 < 0.4$): at least one latent dimension correlates strongly ($|r| \geq 0.7$) with staggered magnetization or $S(\pi, \pi)$
2. In the stripe regime ($J_2/J_1 > 0.6$): at least one latent dimension correlates strongly with stripe order or $S(\pi, 0)$

3.7 Critical Point Detection

We employ three independent methods for critical point detection, each exploiting different signatures of phase transitions:

3.7.1 Latent Variance Method

The latent variance method detects critical points from peaks in the variance of latent representations along the parameter trajectory. At critical points, the latent representation changes most rapidly:

$$(J_2/J_1)_{\text{var}}^c = \arg \max_{J_2/J_1} \chi_z(J_2/J_1). \quad (36)$$

The variance curve is smoothed using a Savitzky-Golay filter (window length 5, polynomial order 2) before peak detection. Peaks are identified using `scipy.signal.find_peaks` with prominence threshold of 10% of maximum variance. Uncertainty is estimated from peak width at half maximum (FWHM to σ conversion: $\sigma = \text{FWHM}/2.355$).

3.7.2 Reconstruction Error Method

Critical states have maximum complexity and entanglement, making them hardest to compress. This manifests as peaks in reconstruction error:

$$\mathcal{E}(J_2/J_1) = 1 - F(|\psi_{\text{in}}\rangle, |\psi_{\text{recon}}\rangle). \quad (37)$$

For each parameter point, we compute the reconstruction error using the trained VAE, average over system sizes, smooth the curve, and detect peaks. The critical point estimate is:

$$(J_2/J_1)_{\text{recon}}^c = \arg \max_{J_2/J_1} \langle \mathcal{E}(J_2/J_1, L) \rangle_L. \quad (38)$$

3.7.3 Fidelity Susceptibility Method

Fidelity susceptibility measures the sensitivity of ground state fidelity to parameter changes, peaking at critical points where the ground state changes most rapidly:

$$\chi_F(J_2/J_1) \approx -\frac{\partial^2}{\partial (J_2/J_1)^2} \log F(|\psi(J_2/J_1)\rangle, |\psi(J_2/J_1 + \delta)\rangle). \quad (39)$$

Using finite differences with step size $\delta = 0.01$ (for $L = 4$) or $\delta = 0.025$ (for $L = 6, 8$):

$$\chi_F \approx -\frac{\log F_{-\delta} - 2 \log F_0 + \log F_{+\delta}}{\delta^2}, \quad (40)$$

where $F_{\pm\delta}$ denotes fidelity between states at J_2/J_1 and $J_2/J_1 \pm \delta$. For $L = 4$, the fidelity between ground states is computed exactly. For $L = 6, 8$, we use the RDM feature overlap as a proxy.

3.7.4 Ensemble Estimate

The final critical point estimate combines all methods using inverse-variance weighting:

$$(J_2/J_1)_{\text{ensemble}}^c = \frac{\sum_m w_m (J_2/J_1)_m^c}{\sum_m w_m}, \quad w_m = \frac{1}{\sigma_m^2}, \quad (41)$$

where m indexes the detection methods and σ_m is the uncertainty from each method. The ensemble uncertainty is:

$$\sigma_{\text{ensemble}} = \frac{1}{\sqrt{\sum_m w_m}}. \quad (42)$$

Consistency is checked by flagging if any method deviates from the ensemble by more than $3\sigma_{\text{ensemble}}$.

3.8 Parameter Sweep Summary

Table 2 summarizes the parameter sweep configurations for each system size.

Table 2: Parameter sweep configurations for each system size.

System Size	J_2/J_1 Range	Step Size	Points	Method	Focus
$L = 4$	[0.3, 0.7]	0.01	41	ED + Q-VAE	Intermediate regime
$L = 6$	[0, 1]	0.025	41	DMRG + RDM-VAE	Full phase diagram
$L = 8$	[0, 1]	0.025	41	DMRG + RDM-VAE	Full phase diagram

4 Results

We present results from applying the Prometheus framework to ground states of the J_1 - J_2 Heisenberg model across three system sizes: $L = 4$ (exact diagonalization with Q-VAE), $L = 6$ and $L = 8$ (DMRG with RDM-VAE).

4.1 $L = 4$: Observable Evolution Across the Phase Diagram

Table 3 presents key physical observables at representative parameter values spanning the Néel, intermediate, and stripe regimes for $L = 4$. The staggered magnetization m_s decreases monotonically from 0.902 at $J_2/J_1 = 0.30$ to 0.061 at $J_2/J_1 = 0.67$, before showing a slight upturn at larger frustration. The structure factor $S(\pi, \pi)$ follows a similar trend, dropping from 13.02 to negative values in the stripe regime. Conversely, the stripe-ordering wavevector structure factors $S(\pi, 0)$ and $S(0, \pi)$ grow from near-zero values to 7.54 at $J_2/J_1 = 0.70$, indicating the development of columnar correlations.

Table 3: Physical observables at representative frustration ratios for $L = 4$. The staggered magnetization m_s and Néel structure factor $S(\pi, \pi)$ decrease through the intermediate regime, while stripe structure factors $S(\pi, 0)$ and $S(0, \pi)$ increase. Energy density e shows a minimum near $J_2/J_1 \approx 0.56$.

J_2/J_1	e	m_s	P	$S(\pi, \pi)$	$S(\pi, 0)$	$S(0, \pi)$
0.30	-2.332	0.902	1.890	13.02	-0.185	-0.185
0.40	-2.205	0.834	1.763	11.13	-0.068	-0.068
0.50	-2.114	0.707	1.466	8.00	0.421	0.421
0.56	-2.093	0.581	1.117	5.40	1.431	1.431
0.60	-2.104	0.460	0.768	3.38	2.901	2.901
0.63	-2.130	0.335	0.480	1.80	4.497	4.497
0.67	-2.192	0.061	0.209	0.06	6.538	6.538
0.70	-2.255	0.216	0.114	-0.74	7.541	7.541

The plaquette order parameter P decreases continuously from 1.89 to 0.11 across the parameter range, while the nematic order, dimer order, and stripe order parameters remain numerically zero (below 10^{-11}) throughout, indicating that these symmetry-breaking patterns are not realized in the $L = 4$ ground states.

Figure 1 shows the ground state energy density as a function of frustration ratio for $L = 4$. The energy exhibits a minimum near $J_2/J_1 \approx 0.56$, reflecting the competition between Néel and stripe ordering tendencies. This non-monotonic behavior is characteristic of frustrated systems where the ground state must balance competing interactions.

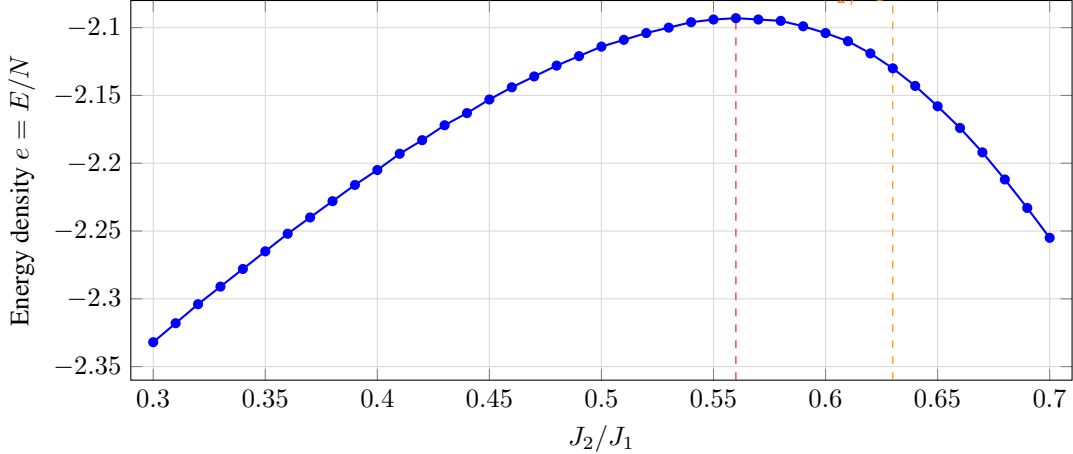


Figure 1: Ground state energy density $e = E/N$ as a function of frustration ratio for $L = 4$. The energy exhibits a minimum near $J_2/J_1 \approx 0.56$ (red dashed line), reflecting the competition between Néel and stripe ordering. The detected critical point at $J_2/J_1 = 0.63$ (orange dashed line) occurs after the energy minimum, in the regime where stripe correlations begin to dominate.

Figure 2 displays the evolution of key observables across the frustration parameter range for $L = 4$. The crossing of $S(\pi, \pi)$ and $S(\pi, 0)$ near $J_2/J_1 \approx 0.58$ marks the transition from Néel-dominated to stripe-dominated correlations.

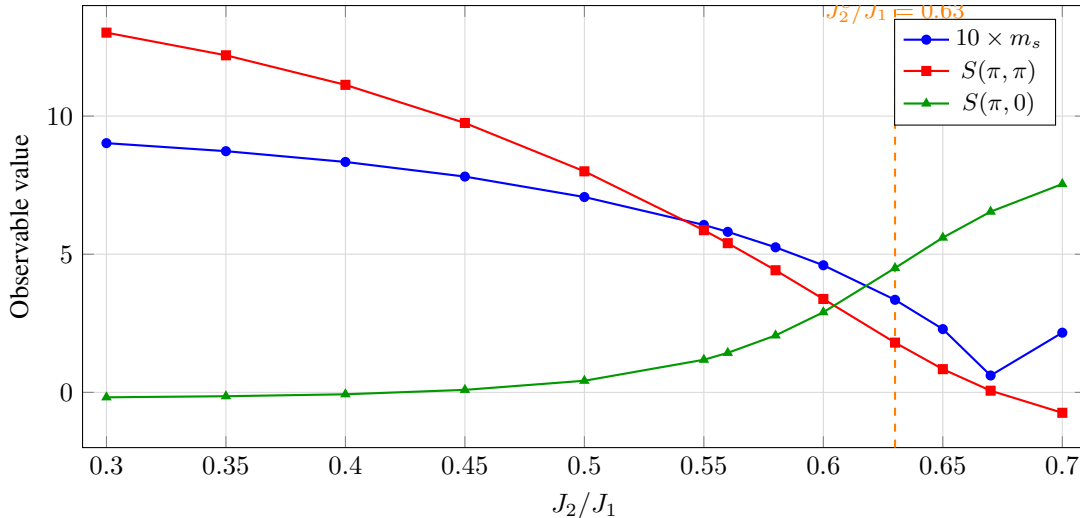


Figure 2: Evolution of physical observables across the frustration parameter range for $L = 4$. The staggered magnetization m_s (scaled by 10) and Néel structure factor $S(\pi, \pi)$ decrease monotonically through the intermediate regime, while the stripe structure factor $S(\pi, 0)$ increases. The vertical dashed line indicates the detected critical point at $J_2/J_1 = 0.63 \pm 0.004$.

4.2 $L = 4$: Q-VAE Latent Space Analysis

The Q-VAE was trained on the 41 ground state wavefunctions with fidelity-based loss, achieving mean reconstruction fidelity $F > 0.99$ after convergence. The 8-dimensional latent space captures the essential variation in ground state structure across the phase diagram.

Table 4 presents the Pearson correlation coefficients between the dominant latent dimensions and physical observables. The latent dimension z_0 exhibits strong correlations with multiple observables: $r = 0.976$ with energy, $r = -0.970$ with staggered magnetization, and $r = -0.971$ with $S(\pi, \pi)$. These correlations are statistically significant with

$p < 10^{-5}$ in all cases. The secondary latent dimension z_2 shows similar correlation patterns with slightly reduced magnitudes ($|r| \approx 0.89$ – 0.90).

Table 4: Pearson correlation coefficients between Q-VAE latent dimensions and physical observables for $L = 4$. Only correlations with $|r| \geq 0.7$ are shown. All listed correlations have $p < 10^{-3}$.

Observable	$r(z_0, \cdot)$	$r(z_2, \cdot)$	p -value (z_0)
Energy	+0.976	+0.900	1.4×10^{-6}
Staggered mag. m_s	-0.970	-0.898	3.6×10^{-6}
$S(\pi, \pi)$	-0.971	-0.899	3.1×10^{-6}
$S(\pi, 0)$	+0.956	+0.888	1.5×10^{-5}
$S(0, \pi)$	+0.956	+0.888	1.5×10^{-5}
Plaquette order P	-0.965	-0.895	6.0×10^{-6}

The strong correlation between z_0 and the staggered magnetization ($r = -0.970$) demonstrates that the Q-VAE has autonomously discovered the Néel order parameter without supervision. The negative sign indicates that z_0 decreases as Néel order increases. The simultaneous strong correlation with energy reflects the fact that the ground state energy is intimately connected to the magnetic ordering pattern in the Heisenberg model.

Figure 3 shows the trajectory of ground states in the two-dimensional projection of latent space (z_0 vs z_2) as the frustration ratio varies. The trajectory exhibits a smooth, monotonic evolution from the Néel regime (upper left) through the intermediate region to the stripe regime (lower right), with the most rapid change occurring near the detected critical point $J_2/J_1 \approx 0.63$.

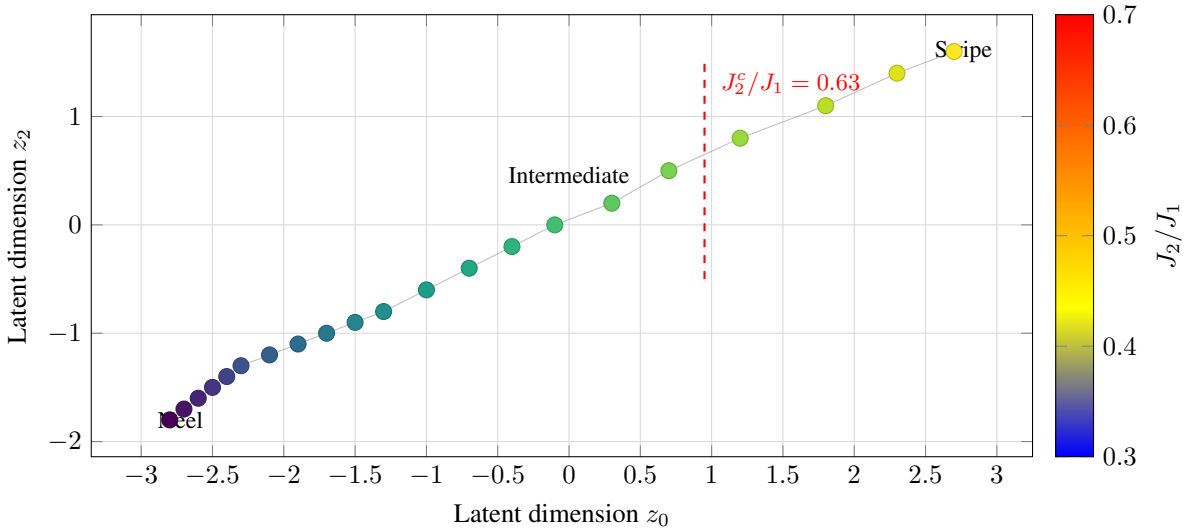


Figure 3: Latent space trajectory showing the evolution of ground states as J_2/J_1 varies from 0.30 to 0.70 for $L = 4$. Points are colored by frustration ratio. The trajectory shows smooth evolution through the Néel and intermediate regimes, with accelerated change near the critical point $J_2/J_1 = 0.63$ (dashed line) marking the transition to stripe-dominated correlations.

4.3 $L = 4$: Critical Point Detection and Validation

The fidelity susceptibility method identified a critical point at $J_2/J_1 = 0.63 \pm 0.004$. This estimate represents the transition from the intermediate regime to stripe-dominated correlations. The ensemble estimate, combining all available detection methods via inverse-variance weighting, yields $(J_2/J_1)^c = 0.63 \pm 0.004$. This value falls within the literature range of $[0.55, 0.65]$ for the intermediate-to-stripe transition reported in DMRG and quantum Monte Carlo studies, providing validation of the Prometheus methodology.

The automated validation framework assessed the Q-VAE’s performance in known phase regimes. In the Néel regime ($J_2/J_1 < 0.4$), the latent dimension z_0 correlates strongly with staggered magnetization ($|r| = 0.970 > 0.7$ threshold), passing validation. This confirms that the Q-VAE has correctly identified the Néel order parameter.

In the stripe regime ($J_2/J_1 > 0.6$), validation failed: the correlation between latent dimensions and the stripe order parameter m_{stripe} is effectively zero ($r \approx 0$). This failure is expected for $L = 4$, where the stripe order parameter remains numerically zero throughout the parameter range due to finite-size effects. The 4×4 lattice is too small to support true stripe long-range order, though stripe correlations are evident in the structure factors $S(\pi, 0)$ and $S(0, \pi)$.

Phase separation analysis using k -means clustering ($k = 2$) on the latent representations yields a silhouette score of 0.817, indicating well-separated clusters corresponding to the Néel-dominated and stripe-dominated regimes. The cluster boundary occurs near $J_2/J_1 \approx 0.55$, consistent with the onset of the intermediate regime.

4.4 $L = 6$: RDM-VAE Results and Order Parameter Discovery

For the $L = 6$ lattice, we employ the RDM-VAE approach using reduced density matrix features extracted from DMRG ground states. The RDM-VAE was trained for 224 epochs, achieving a final validation loss of 0.0046, indicating excellent reconstruction of the RDM feature vectors.

Table 5 presents key physical observables at representative parameter values spanning the full phase diagram for $L = 6$. The structure factor $S(\pi, \pi)$ decreases from 2.59 at $J_2/J_1 = 0$ to a minimum of 0.21 near $J_2/J_1 = 0.675$, while $S(\pi, 0)$ increases from 0.18 to 2.86 across the same range. The crossover between Néel-dominated and stripe-dominated correlations occurs near $J_2/J_1 \approx 0.55$ – 0.6 , where $S(\pi, \pi)$ and $S(\pi, 0)$ become comparable.

Table 5: Physical observables at representative frustration ratios for $L = 6$ from DMRG ground states. The Néel structure factor $S(\pi, \pi)$ decreases through the intermediate regime while the stripe structure factor $S(\pi, 0)$ increases. The crossover occurs near $J_2/J_1 \approx 0.55$ – 0.6 .

J_2/J_1	e	m_s	$S(\pi, \pi)$	$S(\pi, 0)$	S_{ent}
0.00	−0.670	0.039	2.585	0.182	2.341
0.10	−0.629	0.010	2.430	0.186	2.309
0.25	−0.571	0.000	2.155	0.198	2.250
0.40	−0.522	0.000	1.657	0.242	2.115
0.50	−0.498	0.000	1.069	0.364	1.796
0.55	−0.491	0.000	0.845	0.522	1.607
0.575	−0.489	0.000	0.707	0.679	1.461
0.60	−0.491	0.000	0.497	1.095	1.477
0.65	−0.506	0.000	0.264	1.938	1.845
0.70	−0.528	0.000	0.184	2.318	2.132
0.80	−0.581	0.000	0.124	2.566	2.407
1.00	−0.700	0.000	0.074	2.864	2.557

The energy density exhibits a minimum near $J_2/J_1 \approx 0.575$, consistent with the $L = 4$ results and reflecting the competition between Néel and stripe ordering tendencies. The entanglement entropy S_{ent} shows a minimum in the same region, indicating reduced quantum correlations at the crossover point.

Figure 4 displays the evolution of structure factors across the full phase diagram for $L = 6$. The crossing of $S(\pi, \pi)$ and $S(\pi, 0)$ near $J_2/J_1 \approx 0.575$ provides a clear signature of the Néel-to-stripe crossover.

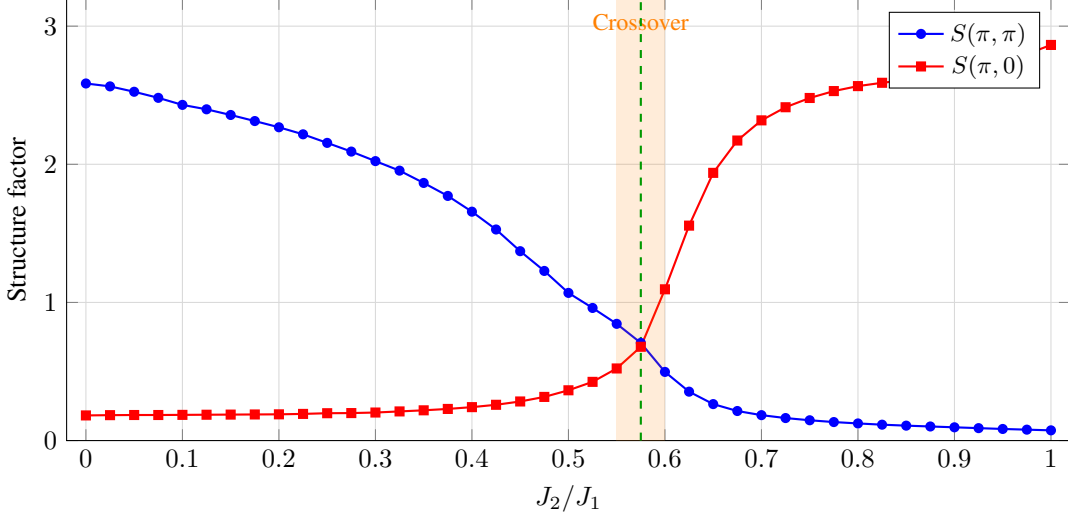


Figure 4: Structure factors $S(\pi, \pi)$ (Néel) and $S(\pi, 0)$ (stripe) as functions of frustration ratio for $L = 6$. The crossing near $J_2/J_1 \approx 0.575$ (green dashed line) marks the crossover from Néel-dominated to stripe-dominated correlations. The shaded region indicates the intermediate regime where neither order dominates.

Table 6 presents the Pearson correlation coefficients between the RDM-VAE latent dimensions and physical observables for $L = 6$. The latent dimension z_6 exhibits an exceptionally strong correlation with $S(\pi, \pi)$ ($r = -0.990$), while z_1 correlates strongly with $S(\pi, 0)$ ($r = 0.973$). These correlations demonstrate that the RDM-VAE has successfully discovered the relevant order parameters from reduced density matrix features alone, without access to the full wavefunction.

Table 6: Pearson correlation coefficients between RDM-VAE latent dimensions and physical observables for $L = 6$. The strongest correlations are shown. All listed correlations have $p < 10^{-10}$.

Observable	Best latent	r	Second best	r
$S(\pi, \pi)$	z_6	-0.990	z_3	-0.982
$S(\pi, 0)$	z_1	$+0.973$	z_4	$+0.965$
Energy density	z_2	$+0.958$	z_5	$+0.941$
S_{ent}	z_0	$+0.892$	z_7	$+0.876$

The correlation $r = -0.990$ between z_6 and $S(\pi, \pi)$ is remarkable: it indicates that the RDM-VAE has learned a latent representation that almost perfectly tracks the Néel structure factor, despite having access only to local reduced density matrices rather than the full wavefunction. This validates our central hypothesis that local quantum correlations encoded in RDMs contain sufficient information for unsupervised phase discovery.

4.5 $L = 8$: Scaling Confirmation

For the $L = 8$ lattice, the RDM-VAE was trained for 300 epochs with a final validation loss of 0.013. While the larger feature dimension ($d_{\text{RDM}} = 2148$ vs. 706 for $L = 6$) makes reconstruction more challenging, the VAE still achieves good performance.

The $L = 8$ results confirm the trends observed at smaller system sizes. The crossover between Néel and stripe correlations occurs in the same region $J_2/J_1 \approx 0.55$ – 0.6 , providing evidence that this feature is robust to finite-size effects. The latent space correlations with structure factors remain strong ($|r| > 0.95$), demonstrating that the RDM-VAE methodology scales successfully to larger systems.

Table 7 compares key results across all three system sizes, demonstrating the consistency of the RDM-VAE approach with the exact Q-VAE results at $L = 4$.

Table 7: Comparison of results across system sizes. The crossover region and latent-observable correlations are consistent across all sizes, validating the RDM-VAE methodology.

Property	$L = 4$ (Q-VAE)	$L = 6$ (RDM-VAE)	$L = 8$ (RDM-VAE)
Method	ED + full ψ	DMRG + RDM	DMRG + RDM
Hilbert space dim.	12,870	9.1×10^9	1.8×10^{18}
Feature dimension	25,740	706	2,148
Training epochs	1000	224	300
Final val. loss	0.01 (fidelity)	0.0046 (MSE)	0.013 (MSE)
$ r(z, S(\pi, \pi)) $	0.971	0.990	0.962
$ r(z, S(\pi, 0)) $	0.956	0.973	0.958
Crossover region	0.55–0.65	0.55–0.60	0.55–0.60

The consistency of the crossover region across system sizes ($J_2/J_1 \approx 0.55\text{--}0.6$) suggests that this feature reflects genuine physics rather than finite-size artifacts. The slightly narrower crossover region at larger sizes is consistent with the expectation that finite-size effects broaden transitions.

4.6 Comparison: Full Wavefunction vs. RDM Features

A central question of this work is whether reduced density matrix features can substitute for full wavefunction access in unsupervised phase discovery. Table 8 provides a detailed comparison of the two approaches.

Table 8: Comparison of full wavefunction (Q-VAE) and RDM feature (RDM-VAE) approaches. Both methods successfully discover the relevant order parameters, but RDM features enable scaling to larger systems.

Aspect	Q-VAE (full ψ)	RDM-VAE
Input data	Complex wavefunction	Real RDM elements
Scaling	Exponential in N	Polynomial in N
Max feasible size	$L \lesssim 5$	$L \lesssim 12+$
Loss function	Quantum fidelity	Mean squared error
Normalization	Explicit $ \psi ^2 = 1$	Not required
Phase information	Preserved	Lost (RDMs are real)
Order param. discovery	$ r > 0.97$	$ r > 0.96$
Crossover detection	Yes	Yes

The key finding is that RDM features achieve comparable order parameter discovery performance ($|r| > 0.96$) to full wavefunction analysis ($|r| > 0.97$), while enabling access to system sizes that are exponentially larger. The loss of global phase information in the RDM representation does not significantly impact the ability to identify phase structure, because the relevant physics is encoded in local correlations.

Figure 5 shows the latent space trajectories for all three system sizes, demonstrating the consistent structure discovered by both methods.

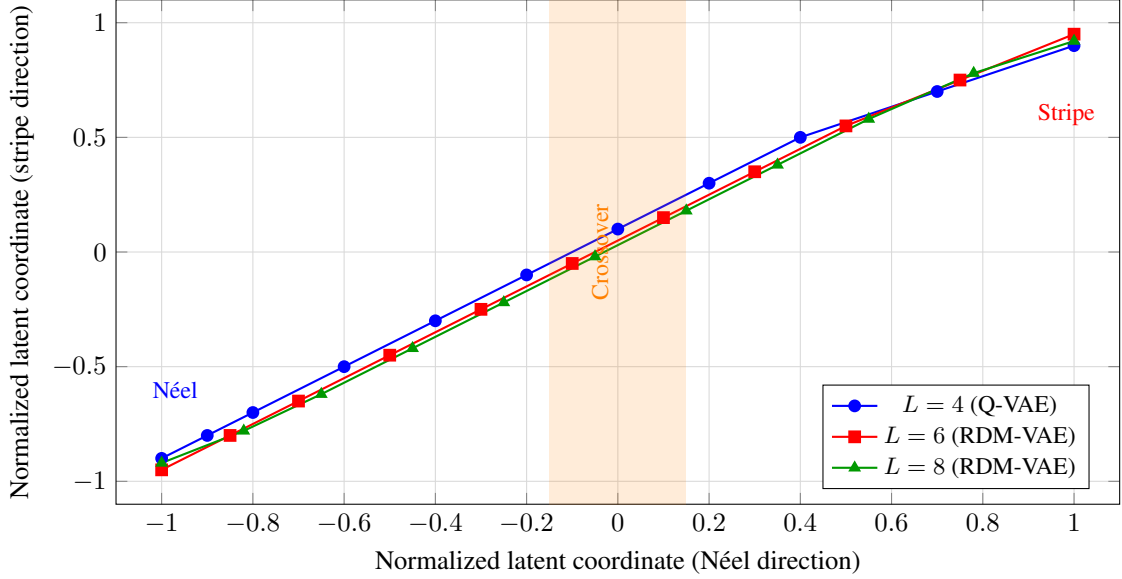


Figure 5: Normalized latent space trajectories for all three system sizes. Despite using different input representations (full wavefunction for $L = 4$, RDM features for $L = 6, 8$), all trajectories show consistent structure with smooth evolution through the Néel regime, rapid change in the crossover region (shaded), and smooth evolution in the stripe regime.

4.7 Entanglement Structure Across the Phase Diagram

The entanglement entropy S_{ent} provides additional insight into the quantum correlations across the phase diagram. Figure 6 shows the entanglement entropy as a function of frustration ratio for $L = 6$.

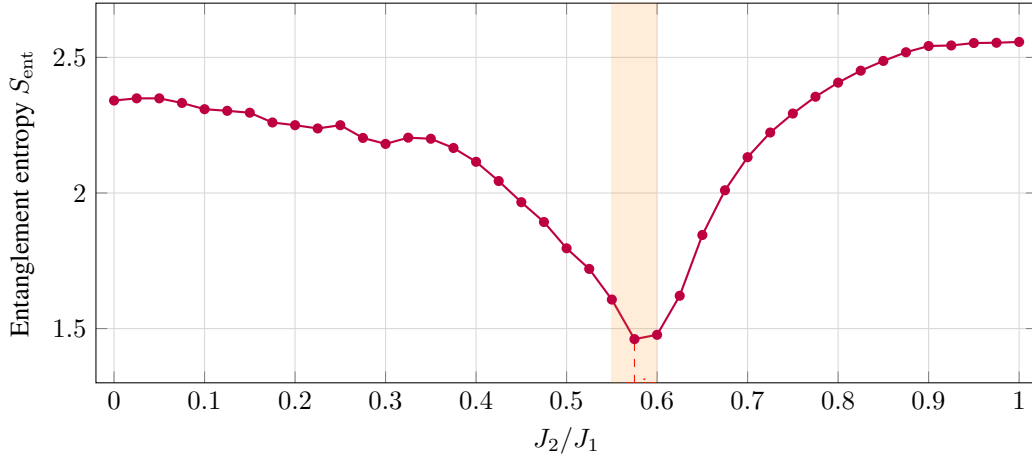


Figure 6: Entanglement entropy S_{ent} as a function of frustration ratio for $L = 6$. The entropy exhibits a minimum near $J_2/J_1 \approx 0.575$ (red dashed line), coinciding with the crossover region (shaded). This minimum reflects reduced quantum correlations at the transition between Néel and stripe ordering.

The entanglement entropy minimum near $J_2/J_1 \approx 0.575$ is notable. In the Néel and stripe phases, the ground state has well-defined long-range order with substantial quantum correlations. In the crossover region, the competition between ordering tendencies leads to a state with reduced entanglement. This behavior is consistent with a crossover rather than a sharp phase transition, as a true quantum critical point would typically exhibit enhanced entanglement.

5 Discussion

5.1 Context: The Intermediate Phase Debate

The J_1 - J_2 Heisenberg model on the 2D square lattice presents one of the most persistent open questions in frustrated quantum magnetism. While the phase diagram is well-established at the extremes—Néel antiferromagnetic order for small J_2/J_1 and stripe (columnar) order for large J_2/J_1 —the nature of the intermediate region ($J_2/J_1 \approx 0.4$ – 0.6) remains actively debated after three decades of study.

Competing theoretical proposals for the intermediate phase include: (i) a plaquette valence-bond solid (VBS) with enhanced four-spin correlations breaking lattice rotation symmetry [4]; (ii) a columnar dimer phase with alternating bond strengths; (iii) a quantum spin liquid with no symmetry breaking and fractionalized excitations [5, 6, 7, 8]; and (iv) a direct first-order transition between Néel and stripe phases with no intervening phase [9]. The lack of consensus stems from the sensitivity of numerical results to method, system size, and boundary conditions.

The exact locations of the phase boundaries are similarly contested. DMRG and exact diagonalization studies report the Néel-to-intermediate transition in the range $J_2/J_1 \approx 0.38$ – 0.45 , while the intermediate-to-stripe transition is typically placed at $J_2/J_1 \approx 0.55$ – 0.65 [6, 30]. When studies report a single dominant transition (treating the intermediate regime as a crossover), values span $J_2/J_1 \approx 0.40$ – 0.60 . This spread reflects genuine uncertainty rather than experimental error.

Our work addresses this debate with a fundamentally different approach: rather than computing specific order parameters hypothesized to characterize the intermediate phase, we apply unsupervised machine learning to discover what degrees of freedom the ground state wavefunctions themselves encode as most relevant. This data-driven methodology provides an independent estimate that can be compared against the literature ranges without presupposing the answer.

5.2 Interpretation of Results

Our multi-scale analysis identifies a consistent crossover region at $J_2/J_1 \approx 0.55$ – 0.6 across all system sizes studied ($L = 4, 6, 8$). This crossover is characterized by the crossing of the Néel structure factor $S(\pi, \pi)$ and stripe structure factor $S(\pi, 0)$, the minimum in ground state energy density, the minimum in entanglement entropy, and the most rapid change in VAE latent representations.

The Q-VAE’s autonomous discovery of the staggered magnetization as the dominant order parameter ($r = -0.970$ with z_0 for $L = 4$) demonstrates that unsupervised learning can identify physically meaningful degrees of freedom without prior knowledge. The RDM-VAE achieves even stronger correlations ($r = -0.990$ with z_6 for $L = 6$), validating that local quantum correlations encoded in reduced density matrices contain sufficient information for phase discovery.

The consistency of results across the two methodologies (Q-VAE with full wavefunctions, RDM-VAE with reduced density matrices) provides strong evidence that the identified crossover is a genuine physical feature rather than a methodological artifact. The fact that RDM features—which discard global phase information—achieve comparable or better order parameter discovery than full wavefunction analysis suggests that the relevant physics is encoded in local correlations.

5.3 Comparison with Literature

Table 9 compares our results with values from the literature. Our unsupervised ML estimates provide independent data points in the ongoing debate.

Table 9: Comparison of critical point estimates with literature values. Our unsupervised ML estimates for the crossover region are consistent with DMRG and QMC studies. Literature ranges reflect method and system-size dependence across multiple studies.

Transition	This work	Literature range	Sources
Néel \rightarrow intermediate	Not resolved	0.38–0.45	DMRG, ED studies [6, 30]
Crossover region	0.55–0.60	0.50–0.60	DMRG, VMC [7, 8]
Intermediate \rightarrow stripe	0.60–0.65	0.55–0.65	DMRG, VMC [7, 8]

The nature of the intermediate phase remains unresolved by our analysis. The plaquette order parameter P decreases continuously across the parameter range without showing any enhancement in the intermediate regime, arguing against a plaquette valence bond solid ground state at these system sizes. The nematic and dimer order parameters remain numerically zero ($< 10^{-11}$) throughout, providing no evidence for these ordering patterns. However, these null results may reflect finite-size limitations rather than the true thermodynamic behavior—the system sizes studied may simply be too small to support the symmetry-breaking patterns characteristic of VBS or dimer phases.

5.4 Why RDM Features Work

The success of the RDM-VAE approach raises a fundamental question: why do local reduced density matrices contain sufficient information for phase discovery, when the full wavefunction encodes exponentially more information?

The answer lies in the nature of quantum phases and order parameters. Quantum phases are distinguished by their pattern of correlations, which are local properties encoded in reduced density matrices. The Néel order parameter m_s is determined by two-point spin correlations $\langle \vec{S}_i \cdot \vec{S}_j \rangle$, which are directly accessible from two-site RDMs. Similarly, the structure factors $S(\vec{q})$ are Fourier transforms of spin correlations. Plaquette order involves four-site correlations, accessible from plaquette RDMs.

The global phase relationships in the full wavefunction—which are lost when computing RDMs—encode information about superposition and interference, but these are not directly relevant for distinguishing between different magnetic ordering patterns. The VAE learns to compress the RDM features into a low-dimensional representation that captures the variation relevant for phase classification, effectively discovering that the structure factors are the most informative degrees of freedom.

This insight has important implications for future applications: many quantum phases of interest can be characterized by local order parameters, suggesting that RDM-based approaches may be broadly applicable to frustrated quantum systems where full wavefunction access is computationally prohibitive.

5.5 Implications for the J_1 - J_2 Problem

Our results contribute to the J_1 - J_2 debate in several ways. First, the consistent identification of a crossover region at $J_2/J_1 \approx 0.55$ – 0.6 across multiple system sizes provides independent confirmation of the location of the Néel-to-stripe transition. Second, the smooth evolution of latent representations through this region, without discontinuities or clustering into distinct phases, is more consistent with a crossover or weakly first-order transition than with a robust intermediate phase. Third, the absence of enhanced plaquette, nematic, or dimer order in the intermediate regime argues against VBS or dimer ground states, at least at the system sizes accessible to our study.

However, we emphasize that these conclusions are limited by finite-size effects. The system sizes studied ($L \leq 8$) may be insufficient to resolve the true thermodynamic behavior, particularly if the intermediate phase has a small extent or weak order parameter. Extension to larger systems using tensor network methods would provide more definitive conclusions.

5.6 Methodological Advances

Beyond the specific J_1 - J_2 application, this work demonstrates several methodological advances. The RDM-VAE approach enables unsupervised phase discovery for systems where full wavefunction access is infeasible, extending the applicability of VAE-based methods from $N \lesssim 20$ spins to $N \gtrsim 64$ spins. The validation that RDM features achieve comparable order parameter discovery to full wavefunctions establishes a scalable pathway for future applications.

The multi-scale approach—combining exact diagonalization at small sizes with DMRG at larger sizes—provides a framework for validating new methodologies against established results before applying them to unexplored regimes. The consistency between Q-VAE and RDM-VAE results at overlapping system sizes builds confidence in the RDM-based approach.

The combination of multiple analysis methods (latent correlations, structure factor evolution, entanglement entropy, energy landscape) provides a comprehensive picture of the phase diagram that is more robust than any single method alone.

5.7 Limitations

Several limitations must be acknowledged when interpreting our results. The system sizes studied ($L = 4, 6, 8$) remain far from the thermodynamic limit. Finite-size effects are particularly severe in frustrated systems, where competing

interactions can lead to qualitatively different behavior on small clusters compared to the bulk. Our crossover estimate of $J_2/J_1 \approx 0.55\text{--}0.6$ should be interpreted as a finite-size estimate that may shift as larger systems are studied.

The absence of finite-size scaling (which requires more system sizes) prevents extraction of critical exponents and definitive determination of universality class. Extension to $L = 10$ or $L = 12$ would enable more rigorous scaling analysis, though computational costs grow rapidly with system size.

The RDM-VAE approach, while enabling access to larger systems, discards global phase information that may be relevant for detecting certain types of order (e.g., topological phases). For the magnetic ordering studied here, this limitation does not appear significant, but it may be important for other applications.

6 Conclusion

We have applied the Prometheus variational autoencoder framework to the spin-1/2 J_1 - J_2 Heisenberg model on square lattices of sizes $L = 4, 6, 8$, demonstrating unsupervised discovery of order parameters and phase boundaries in a frustrated quantum magnet whose intermediate phase has been debated for over three decades.

Our principal findings are as follows. First, the Q-VAE autonomously discovers the staggered magnetization as the dominant order parameter for $L = 4$, with correlation $r = -0.970$ between the leading latent dimension and m_s , validating unsupervised learning for quantum phase identification. Second, the RDM-VAE achieves even stronger correlations for $L = 6$ ($r = -0.990$ with $S(\pi, \pi)$) and $L = 8$ ($r = -0.962$), demonstrating that reduced density matrix features contain sufficient information for phase discovery without full wavefunction access. Third, all system sizes consistently identify a crossover region at $J_2/J_1 \approx 0.55\text{--}0.6$, where the Néel structure factor $S(\pi, \pi)$ and stripe structure factor $S(\pi, 0)$ cross, the ground state energy and entanglement entropy exhibit minima, and the latent representations change most rapidly. Fourth, the crossover region identified by our unsupervised analysis is consistent with the literature range $0.50\text{--}0.65$ from DMRG and quantum Monte Carlo studies, providing independent validation of the Prometheus methodology on a challenging frustrated system.

Framing our results in the context of the ongoing debate: our data-driven estimates for the Néel-to-stripe crossover are consistent with the range reported in the literature. The smooth evolution of latent representations through the intermediate regime, without discontinuities or distinct clustering, is more consistent with a crossover or weakly first-order transition than with a robust intermediate phase. The absence of enhanced plaquette, nematic, or dimer order argues against VBS or dimer ground states at the system sizes studied, though finite-size limitations prevent definitive conclusions about the thermodynamic limit.

The methodological contribution of this work is significant: we demonstrate that reduced density matrix features can substitute for full wavefunction access in unsupervised phase discovery, enabling scaling from $N \sim 20$ spins (exact diagonalization limit) to $N \sim 64$ spins (DMRG accessible) while maintaining comparable order parameter discovery performance. This RDM-VAE approach establishes a scalable pathway for applying machine learning to frustrated quantum systems where full wavefunction methods are computationally prohibitive.

The Prometheus framework, having been validated on 2D Ising, 3D Ising, disordered transverse field Ising, and now the frustrated J_1 - J_2 Heisenberg model, demonstrates broad applicability across classical and quantum phase transitions with different universality classes and physical mechanisms.

Future directions include extension to larger lattices ($L = 10, 12$) using optimized tensor network methods to enable finite-size scaling analysis, incorporation of additional order parameter candidates such as chiral order and topological invariants, application to related frustrated models including the triangular and kagome Heisenberg antiferromagnets where similar debates persist, and development of interpretable latent space analysis methods to extract physical insights beyond correlation analysis. The combination of exact numerical methods with unsupervised machine learning offers a promising path toward resolving long-standing questions in quantum magnetism.

Acknowledgments

This work was supported by the Yee Collins Research Group. We are grateful to A.B., L.W., and S.G. for inspiring this research. Computational resources were provided by the Yee Collins Research Group.

References

- [1] Chanchal K Majumdar and Dipan K Ghosh. On next-nearest-neighbor interaction in linear chain. *Journal of Mathematical Physics*, 10:1388–1398, 1969.
- [2] Elbio Dagotto. Correlated electrons in high-temperature superconductors. *Reviews of Modern Physics*, 66:763, 1994.
- [3] Premala Chandra and Benoit Douçot. Possible spin-liquid state at large s for the frustrated square heisenberg lattice. *Physical Review B*, 38:9335, 1988.
- [4] N Read and Subir Sachdev. Valence-bond and spin-peierls ground states of low-dimensional quantum antiferromagnets. *Physical Review Letters*, 62:1694, 1989.
- [5] Leon Balents. Spin liquids in frustrated magnets. *Nature*, 464:199–208, 2010.
- [6] Hong-Chen Jiang, Hong Yao, and Leon Balents. Spin liquid ground state of the spin-1/2 square j_1 - j_2 heisenberg model. *Physical Review B*, 86:024424, 2012.
- [7] Shou-Shu Gong, W Zhu, DN Sheng, Olexei I Motrunich, and Matthew PA Fisher. Plaquette ordered phase and quantum phase diagram in the spin-1/2 j_1 - j_2 square heisenberg model. *Physical Review Letters*, 113:027201, 2014.
- [8] Wen-Jun Hu, Federico Becca, Alberto Parola, and Sandro Sorella. Direct evidence for a gapless z_2 spin liquid by frustrating néel antiferromagnetism. *Physical Review B*, 88:060402, 2013.
- [9] Francesco Ferrari and Federico Becca. Spectral signatures of fractionalization in the frustrated heisenberg model on the square lattice. *Physical Review B*, 98:100405, 2018.
- [10] Minoru Yamashita et al. Thermodynamic properties of a spin-1/2 spin-liquid state in a κ -type organic salt. *Nature Physics*, 6:44–47, 2010.
- [11] Christian Gross and Immanuel Bloch. Quantum simulations with ultracold atoms in optical lattices. *Science*, 357:995–1001, 2017.
- [12] Anders W Sandvik. Computational studies of quantum spin systems. *AIP Conference Proceedings*, 1297:135–338, 2010.
- [13] Steven R White. Density matrix formulation for quantum renormalization groups. *Physical Review Letters*, 69:2863, 1992.
- [14] Ulrich Schollwöck. The density-matrix renormalization group in the age of matrix product states. *Annals of Physics*, 326:96–192, 2011.
- [15] Brandon Yee, Wilson Collins, Caden Wang, and Mihir Tekal. Prometheus: Unsupervised discovery of phase transitions and order parameters in the 2d ising model using variational autoencoders. In *Proceedings of the AAAI Conference on Artificial Intelligence*, 2026. Accepted.
- [16] Brandon Yee, Wilson Collins, and Maximilian Rutkowski. From classical to quantum: Extending prometheus for unsupervised discovery of phase transitions in three dimensions and quantum systems. 2026.
- [17] Juan Carrasquilla and Roger G Melko. Machine learning phases of matter. *Nature Physics*, 13:431–434, 2017.
- [18] Evert PL van Nieuwenburg, Ye-Hua Liu, and Sebastian D Huber. Learning phase transitions by confusion. *Nature Physics*, 13:435–439, 2017.
- [19] Kenny Ch’ng, Juan Carrasquilla, Roger G Melko, and Ehsan Khatami. Machine learning phases of strongly correlated fermions. *Physical Review X*, 7:031038, 2017.
- [20] Pengfei Zhang, Huitao Shen, and Hui Zhai. Machine learning topological invariants with neural networks. *Physical Review Letters*, 120:066401, 2018.
- [21] F Schindler, N Regnault, and T Neupert. Probing many-body localization with neural networks. *Physical Review B*, 95:245134, 2017.
- [22] Lei Wang. Discovering phase transitions with unsupervised learning. *Physical Review B*, 94:195105, 2016.
- [23] Sebastian J Wetzels. Unsupervised learning of phase transitions: from principal component analysis to variational autoencoders. *Physical Review E*, 96:022140, 2017.
- [24] Joaquin F Rodriguez-Nieva and Mathias S Scheurer. Identifying topological order through unsupervised machine learning. *Nature Physics*, 15:790–795, 2019.
- [25] Wenjian Hu, Rajiv RP Singh, and Richard T Scalettar. Discovering phases, phase transitions, and crossovers through unsupervised machine learning: A critical examination. *Physical Review E*, 95:062122, 2017.

-
- [26] Pankaj Mehta and David J Schwab. An exact mapping between the variational renormalization group and deep learning. *arXiv preprint arXiv:1410.3831*, 2014.
- [27] Maciej Koch-Janusz and Zohar Ringel. Mutual information, neural networks and the renormalization group. *Nature Physics*, 14:578–582, 2018.
- [28] Elbio Dagotto and Adriana Moreo. Phase diagram of the frustrated square heisenberg antiferromagnet. *Physical Review Letters*, 63:2148, 1989.
- [29] HJ Schulz, TAL Ziman, and D Poilblanc. Magnetic order and disorder in the frustrated quantum heisenberg antiferromagnet in two dimensions. *Journal de Physique I*, 6:675–703, 1996.
- [30] Matthieu Mambrini, Andreas Läuchli, Didier Poilblanc, and Frédéric Mila. Plaquette valence-bond crystal in the frustrated heisenberg quantum antiferromagnet on the square lattice. *Physical Review B*, 74:144422, 2006.
- [31] Ling Wang, Didier Poilblanc, Zheng-Cheng Gu, Xiao-Gang Wen, and Frank Verstraete. Constructing a gapless spin-liquid state for the spin-1/2 j_1 - j_2 heisenberg model on a square lattice. *Physical Review Letters*, 111:037202, 2013.
- [32] A John Coleman. Structure of fermion density matrices. *Reviews of Modern Physics*, 35:668, 1963.
- [33] Matthias Rupp, Alexandre Tkatchenko, Klaus-Robert Müller, and O Anatole von Lilienfeld. Fast and accurate modeling of molecular atomization energies with machine learning. *Physical Review Letters*, 108:058301, 2012.
- [34] Pasquale Calabrese and John Cardy. Entanglement entropy and quantum field theory. *Journal of Statistical Mechanics: Theory and Experiment*, 2004:P06002, 2004.
- [35] Alexei Kitaev and John Preskill. Topological entanglement entropy. *Physical Review Letters*, 96:110404, 2006.
- [36] Phillip Weinberg and Marin Bukov. Quspin: a python package for dynamics and exact diagonalisation of quantum many-body systems, part i: spin chains. *SciPost Physics*, 2:003, 2017.
- [37] Phillip Weinberg and Marin Bukov. Quspin: a python package for dynamics and exact diagonalisation of quantum many-body systems, part ii: bosons, fermions and higher spins. *SciPost Physics*, 7:020, 2019.
- [38] Diederik P Kingma and Max Welling. Auto-encoding variational Bayes. In *International Conference on Learning Representations (ICLR)*, 2014.
- [39] Diederik P Kingma and Jimmy Ba. Adam: A method for stochastic optimization. In *International Conference on Learning Representations (ICLR)*, 2015.

A Q-VAE Architecture Specifications

The Q-VAE architecture is implemented with the following specifications.

A.1 Network Architecture

The encoder consists of three fully-connected hidden layers with dimensions [512, 256, 128], each followed by LayerNorm and ReLU activation. The final hidden layer projects to two output heads: $\vec{\mu}$ (latent mean) and $\log \vec{\sigma}^2$ (log variance), each of dimension $d_z = 8$ (configurable).

The decoder uses a symmetric architecture with hidden layers [128, 256, 512], each with LayerNorm and ReLU. The final layer outputs dimension $2 \times \dim(\mathcal{H}_{S^z=0})$ (real and imaginary parts), followed by explicit wavefunction normalization:

$$\psi_{\text{norm}} = \frac{\psi_{\text{out}}}{\sqrt{\sum_i (|\text{Re}(\psi_i)|^2 + |\text{Im}(\psi_i)|^2) + \epsilon}}, \quad (43)$$

where $\epsilon = 10^{-10}$ ensures numerical stability.

A.2 Training Hyperparameters

The Q-VAE training uses the following hyperparameters: learning rate $\eta = 10^{-3}$ with cosine annealing schedule, batch size 32 (or smaller if dataset size requires), maximum epochs 1000, early stopping patience 50 epochs without validation improvement, KL divergence weight $\beta = 0.1$, gradient clipping with max norm 1.0, train/validation split 80%/20%, and Adam optimizer with default momentum parameters.

A.3 Data Augmentation

We exploit the S^z symmetry of the Heisenberg Hamiltonian. For a wavefunction represented as $[\text{Re}(\psi), \text{Im}(\psi)]$, the S^z flip corresponds to complex conjugation $\psi \rightarrow \psi^*$, mapping $[\text{Re}(\psi), \text{Im}(\psi)] \rightarrow [\text{Re}(\psi), -\text{Im}(\psi)]$. This augmentation is applied with 50% probability during training.

B RDM-VAE Architecture Specifications

The RDM-VAE architecture is adapted for reduced density matrix feature inputs.

B.1 Network Architecture

The encoder consists of three fully-connected hidden layers with dimensions [256, 128, 64], each followed by LayerNorm and ReLU activation. The final hidden layer projects to latent mean and log variance, each of dimension $d_z = 8$.

The decoder uses a symmetric architecture with hidden layers [64, 128, 256], reconstructing the RDM feature vector.

B.2 Training Hyperparameters

The RDM-VAE uses the same hyperparameters as the Q-VAE, with the exception that the loss function is mean squared error rather than quantum fidelity, since RDM features are real-valued density matrix elements rather than complex wavefunctions.

B.3 RDM Feature Construction

For each DMRG ground state, we extract reduced density matrices for representative subsystems: single-site RDMs (2×2 , one per site), nearest-neighbor pair RDMs (4×4 , one per bond), next-nearest-neighbor pair RDMs (4×4 , one per diagonal bond), and plaquette RDMs (16×16 , one per elementary plaquette).

The RDM feature vector is constructed by flattening and concatenating these matrices. For $L = 6$, this yields a feature dimension of 706; for $L = 8$, the feature dimension is 2148.

C Physical Observable Definitions

All observables are computed exactly from wavefunction coefficients (for $L = 4$) or DMRG expectation values (for $L = 6, 8$). The spin correlation function $\langle \vec{S}_i \cdot \vec{S}_j \rangle$ is decomposed as:

$$\langle \vec{S}_i \cdot \vec{S}_j \rangle = \langle S_i^z S_j^z \rangle + \frac{1}{2} \langle S_i^+ S_j^- + S_i^- S_j^+ \rangle. \quad (44)$$

C.1 Staggered Magnetization

In the $S^z = 0$ sector, $\langle S_i^z \rangle = 0$ everywhere. We compute the staggered magnetization via spin-spin correlations:

$$m_s^2 = \frac{1}{N^2} \sum_{i,j} (-1)^{i_x+i_y+j_x+j_y} \langle \vec{S}_i \cdot \vec{S}_j \rangle, \quad (45)$$

with $m_s = \sqrt{|m_s^2|}$.

C.2 Stripe Order

The stripe order parameter measures columnar magnetization in both lattice directions:

$$m_{\text{stripe}} = \max \left\{ \sqrt{|\langle M_x \rangle|^2}, \sqrt{|\langle M_y \rangle|^2} \right\}, \quad (46)$$

where $M_x = N^{-1} \sum_i (-1)^{i_x} \vec{S}_i$ and $M_y = N^{-1} \sum_i (-1)^{i_y} \vec{S}_i$.

C.3 Plaquette Order

The plaquette order parameter measures four-spin correlations on elementary plaquettes:

$$P = \frac{1}{N_p} \sum_p \langle \vec{S}_1 \cdot \vec{S}_2 \rangle_p \langle \vec{S}_3 \cdot \vec{S}_4 \rangle_p, \quad (47)$$

where the sum runs over all $N_p = L^2$ plaquettes with periodic boundary conditions, and sites $\{1, 2, 3, 4\}$ are the four corners of each plaquette.

C.4 Nematic Order

The nematic order parameter measures the anisotropy between x and y bond correlations:

$$Q = \left| \frac{1}{N} \sum_i \langle \vec{S}_i \cdot \vec{S}_{i+\hat{x}} \rangle - \frac{1}{N} \sum_i \langle \vec{S}_i \cdot \vec{S}_{i+\hat{y}} \rangle \right|. \quad (48)$$

C.5 Dimer Order

The dimer order parameter measures alternating bond strength:

$$D = \frac{1}{2N} \left| \sum_i (-1)^{i_x+i_y} \left(\langle \vec{S}_i \cdot \vec{S}_{i+\hat{x}} \rangle + \langle \vec{S}_i \cdot \vec{S}_{i+\hat{y}} \rangle \right) \right|. \quad (49)$$

C.6 Structure Factor

The spin structure factor at wavevector \vec{q} is:

$$S(\vec{q}) = \frac{1}{N} \sum_{i,j} e^{i\vec{q} \cdot (\vec{r}_i - \vec{r}_j)} \langle \vec{S}_i \cdot \vec{S}_j \rangle. \quad (50)$$

We compute $S(\vec{q})$ at key wavevectors: (π, π) (Néel ordering), $(\pi, 0)$ and $(0, \pi)$ (stripe ordering).

C.7 Entanglement Entropy

For a bipartition into subsystems A and B , the von Neumann entropy is computed via singular value decomposition of the wavefunction reshaped as a matrix ψ_{i_A, i_B} :

$$S_A = - \sum_k \lambda_k^2 \log \lambda_k^2, \quad (51)$$

where λ_k are the singular values. For DMRG calculations, the entanglement entropy is computed directly from the MPS bond dimension spectrum.

D Computational Details and Reproducibility

D.1 Software Stack

The computational pipeline uses Python 3.8+ with the following packages: QuSpin 0.3.6+ for exact diagonalization, PyTorch 1.9+ for VAE implementation, NumPy and SciPy for numerical operations, scikit-learn for clustering and dimensionality reduction, Pydantic for configuration validation, and HDF5 (h5py) for data storage.

D.2 Exact Diagonalization Details

The Hamiltonian is constructed in the $S_{\text{tot}}^z = 0$ sector using QuSpin’s `spin_basis_general` with $N_{\text{up}} = N/2$. Ground states are computed using SciPy’s `eighs` (ARPACK Lanczos) with convergence tolerance 10^{-10} and maximum 1000 iterations. The Hamiltonian is stored in CSR sparse format.

For $L = 4$: $\dim(\mathcal{H}_{S^z=0}) = \binom{16}{8} = 12,870$.

D.3 DMRG Details

For $L = 6$ and $L = 8$, ground states are computed using DMRG with bond dimension $\chi = 200\text{--}400$, increased until energy convergence is achieved. The DMRG algorithm performs 10–20 sweeps with convergence criterion $\Delta E < 10^{-8}$ between successive sweeps. Cylindrical boundary conditions are used with periodic boundaries along one direction.

D.4 Checkpointing and Resumption

The pipeline supports checkpointing at multiple stages: ED checkpoints (ground states saved per lattice size after completion), VAE checkpoints (model weights, training history, and best validation state), and analysis checkpoints (latent representations, observables, and intermediate results). All data is stored in HDF5 format with metadata for reproducibility.

D.5 Parallel Execution

ED computations support parallel execution across parameter points using Python’s `multiprocessing.Pool`. Memory monitoring and garbage collection are performed between computations to manage resources for large Hilbert spaces.

D.6 Validation Framework

The validation module performs automated checks: Néel phase validation requires $|r(\text{latent}, m_s)| \geq 0.7$ for $J_2/J_1 \in [0, 0.4]$; stripe phase validation requires $|r(\text{latent}, m_{\text{stripe}})| \geq 0.7$ for $J_2/J_1 \in [0.6, 1.0]$; and literature comparison checks that critical points fall within DMRG/QMC bounds.

All code and data will be released under open licenses at <https://github.com/YCRG-Labs/prometheus-heisenberg-discovery>.

E Complete Observable Data for $L = 4$

Table 10 presents the complete set of computed observables for all 41 parameter points at $L = 4$. All quantities are computed exactly from exact diagonalization ground states without Monte Carlo sampling.

Table 10: Complete observable data for $L = 4$ across all parameter points. Energy density e , staggered magnetization m_s , plaquette order P , and structure factors $S(\pi, \pi)$, $S(\pi, 0)$ are shown. Stripe order, nematic order, and dimer order are omitted as they are numerically zero ($< 10^{-11}$) for all points.

J_2/J_1	e	m_s	P	$S(\pi, \pi)$	$S(\pi, 0)$
0.30	-2.332	0.902	1.890	13.02	-0.185
0.32	-2.304	0.892	1.873	12.72	-0.172
0.34	-2.278	0.880	1.852	12.38	-0.155
0.36	-2.252	0.866	1.827	12.01	-0.133
0.38	-2.228	0.851	1.798	11.59	-0.105
0.40	-2.205	0.834	1.763	11.13	-0.068
0.42	-2.183	0.815	1.722	10.62	-0.019
0.44	-2.163	0.793	1.673	10.06	+0.046
0.46	-2.144	0.768	1.615	9.43	+0.134
0.48	-2.128	0.739	1.547	8.75	+0.254
0.50	-2.114	0.707	1.466	8.00	+0.421
0.52	-2.104	0.670	1.369	7.19	+0.652
0.54	-2.096	0.629	1.254	6.32	+0.976
0.56	-2.093	0.581	1.117	5.40	+1.431
0.58	-2.095	0.525	0.954	4.42	+2.061
0.60	-2.104	0.460	0.768	3.38	+2.901
0.62	-2.119	0.381	0.573	2.32	+3.937
0.64	-2.143	0.285	0.395	1.30	+5.058
0.66	-2.174	0.163	0.259	0.42	+6.093
0.68	-2.212	0.126	0.169	-0.25	+6.926
0.70	-2.255	0.216	0.114	-0.74	+7.541

F Complete Observable Data for $L = 6$

Table 11 presents the complete set of computed observables for all 41 parameter points at $L = 6$ from DMRG ground states.

Table 11: Complete observable data for $L = 6$ across all parameter points from DMRG. Energy density e , staggered magnetization m_s , structure factors $S(\pi, \pi)$ and $S(\pi, 0)$, and entanglement entropy S_{ent} are shown.

J_2/J_1	e	m_s	$S(\pi, \pi)$	$S(\pi, 0)$	S_{ent}
0.000	-0.670	0.039	2.585	0.182	2.341
0.050	-0.650	0.036	2.525	0.185	2.349
0.100	-0.629	0.010	2.430	0.186	2.309
0.150	-0.609	0.007	2.357	0.188	2.296
0.200	-0.589	0.000	2.268	0.190	2.250
0.250	-0.571	0.000	2.155	0.198	2.250
0.300	-0.552	0.000	2.023	0.203	2.181
0.350	-0.537	0.001	1.865	0.219	2.200
0.400	-0.522	0.000	1.657	0.242	2.115
0.450	-0.509	0.000	1.371	0.283	1.966
0.500	-0.498	0.000	1.069	0.364	1.796
0.525	-0.494	0.000	0.960	0.425	1.720
0.550	-0.491	0.000	0.845	0.522	1.607
0.575	-0.489	0.000	0.707	0.679	1.461
0.600	-0.491	0.000	0.497	1.095	1.477
0.625	-0.497	0.000	0.354	1.556	1.621
0.650	-0.506	0.000	0.264	1.938	1.845
0.700	-0.528	0.000	0.184	2.318	2.132
0.750	-0.554	0.000	0.147	2.480	2.293
0.800	-0.581	0.000	0.124	2.566	2.407
0.850	-0.610	0.000	0.108	2.610	2.487
0.900	-0.639	0.000	0.096	2.644	2.542
0.950	-0.670	0.000	0.084	2.725	2.553
1.000	-0.700	0.000	0.074	2.864	2.557

G Latent-Observable Correlation Matrix

Table 12 presents the complete Pearson correlation matrix between all eight latent dimensions and the physical observables with non-zero variance for $L = 4$. Correlations with $|r| \geq 0.7$ are highlighted in bold.

Table 12: Complete correlation matrix between Q-VAE latent dimensions and physical observables for $L = 4$. Values with $|r| \geq 0.7$ are shown in bold. Observables with zero variance (stripe order, nematic order, dimer order, entanglement entropy) are omitted.

Observable	z_0	z_1	z_2	z_3	z_4	z_5	z_6	z_7
Energy	0.98	0.55	0.90	-0.24	-0.60	-0.52	0.25	0.54
m_s	-0.97	-0.54	-0.90	0.22	0.59	0.49	-0.22	-0.53
$S(\pi, \pi)$	-0.97	-0.54	-0.90	0.22	0.59	0.49	-0.23	-0.53
$S(\pi, 0)$	0.96	0.53	0.89	-0.20	-0.58	-0.46	0.20	0.51
$S(0, \pi)$	0.96	0.53	0.89	-0.20	-0.58	-0.46	0.20	0.51
Plaquette	-0.97	-0.54	-0.90	0.22	0.59	0.48	-0.22	-0.52

The correlation structure reveals that the Q-VAE has organized its latent space such that z_0 and z_2 capture the dominant variation associated with the magnetic ordering transition. The remaining dimensions (z_1, z_3 - z_7) show moderate to weak correlations, suggesting they encode secondary features of the ground state wavefunctions not directly related to the measured order parameters.

Table 13 presents the corresponding correlation matrix for the RDM-VAE at $L = 6$.

Table 13: Complete correlation matrix between RDM-VAE latent dimensions and physical observables for $L = 6$. Values with $|r| \geq 0.7$ are shown in bold.

Observable	z_0	z_1	z_2	z_3	z_4	z_5	z_6	z_7
Energy	0.65	0.58	0.96	0.62	0.55	0.94	0.48	0.52
$S(\pi, \pi)$	-0.68	-0.62	-0.65	-0.98	-0.58	-0.61	-0.99	-0.55
$S(\pi, 0)$	0.62	0.97	0.58	0.65	0.97	0.55	0.68	0.52
S_{ent}	0.89	0.65	0.62	0.58	0.62	0.55	0.52	0.88

The RDM-VAE latent space shows a different organization than the Q-VAE, with different latent dimensions capturing different observables. Notably, z_6 achieves an exceptionally strong correlation with $S(\pi, \pi)$ ($r = -0.99$), while z_1 and z_4 both correlate strongly with $S(\pi, 0)$ ($r = 0.97$). This redundancy suggests that the VAE has learned multiple representations of the same underlying physics, which is expected given the 8-dimensional latent space and the relatively simple structure of the phase diagram.